Marine Geology 408 (2019) 1–17

Contents lists available at ScienceDirect

Marine Geology

journal homepage: www.elsevier.com/locate/margo

Recent, deep-sourced methane/mud discharge at the most active mud volcano in the western Mediterranean

Carmina López-Rodríguez[a,*,1], Gert J. De Lange[b,1], Menchu Comas[a], Francisca Martínez-Ruiz[a], Fernando Nieto[a,c], Célia J. Sapart[d,e], José M. Mogollón[b]

[a] Andalusian Earth Science Institute, CSIC-Granada University, Armilla, Spain
[b] Faculty of Geosciences, Dept. Earth Sciences – Geochemistry, Utrecht University, Utrecht, the Netherlands
[c] Department of Mineralogy and Petrology, University of Granada, Granada, Spain
[d] Institute for Marine and Atmospheric Research, Utrecht University, Utrecht, the Netherlands
[e] Laboratoire de Glaciologie, Université Libre de Bruxelles, Brussels, Belgium

ARTICLE INFO

Keywords:
Alboran Sea
Mud volcanoes
Pore waters
Deep fluids
Isotopes
Clay minerals

ABSTRACT

Active mud volcanism in the West Alboran Basin (WAB) is closely associated with tectonically mobilized, overpressurized shales and shale-diapirism. This appears to control mud expulsion at Carmen mud volcano, a cone-shaped structure 65 m high and 1 km in basal diameter.

The presence of gas-rich mud breccia, living chemosynthetic fauna, the absence of hemipelagic draping and the abrupt transition that occurs between high dissolved sulfate in the uppermost interval and low sulfate together with high methane concentrations in the lowermost sediment interval all point to a recent expulsion of mud breccia at the summit of Carmen MV.

For the lowermost interval, the depletion of major elements (i.e., Ca^{2+} and Mg^{2+}) and the enrichment of trace species (i.e., Li and B) in the pore water all indicate a deep fluid source. The $\delta^{18}O_{pw}$ (5.7‰ VSMOW) and δD_{pw} (−10‰ VSMOW) of pore water in the lowermost interval correspond with smectite dehydration as the main pore-water freshening mechanism. Water-formation temperatures calculated with empirical geo-thermometers (K-Na, K-Mg; $\delta^{18}O_{pw}$, δD_{pw}, and dissolved B) reveal that fluids were generated at temperatures of ~140 ± 20 °C. Taking a regional geothermal gradient for the WAB of 25–27 °C/km, this points to a fluid source from ~5 ± 1 km sediment depth. This is not only consistent with the depth of overpressurized shales and megabreccia of Lower to Middle Miocene age, but it also fits nicely with the Upper/Middle-Miocene seawater value for the porewater $^{87}Sr/^{86}Sr$ derived from dissolving carbonates. The stable carbon and hydrogen isotopic composition of methane ($\delta^{13}C_{methane}$ ~ −59.4‰ VPDB and $\delta D_{methane}$ −184‰ VSMOW) for the deepest samples of summit-core GP05PC is consistent with the mentioned deep origin.

Mud breccia expulsion of overpressurized deep sedimentary units would be accompanied by rigorous degassing, leading to rapid, 'instantaneous' replacement of pore fluid by bottom water in the upper sediments. The absence of oxidized sediment draping, the seawater-like pore-water composition in the uppermost part of the mud breccia interval, and the abrupt methane to sulfate transition all provide evidence for a very recent mud expulsion.

The distinctively kink-shaped pore-water Cl^- profile in core GP05PC has been used in a numerical transport-reaction model to derive the timing for this event. This eruptive event appears to have taken place very recently, namely 12 ± 5 yrs prior to the 2012 coring, thus in the year 2000 CE.

1. Introduction

Mud volcanoes (MVs) have been the target of intensive geochemical and geological studies worldwide, aiming to understand provenance and pathways of their expelled pore fluids and muds. MVs are usually associated with active seepage fields, often dominated by methane

* Corresponding author at: Center for Advanced Studies in Earth Sciences, CEACTierra-University of Jaen, Jaen, Spain.
E-mail addresses: carmina@ugr.es (C. López-Rodríguez), g.j.delange@uu.nl (G.J. De Lange), mcomas@ugr.es (M. Comas), fmruiz@ugr.es (F. Martínez-Ruiz), csapart@ulb.ac.be (C.J. Sapart), j.m.mogollonlee@uu.nl (J.M. Mogollón).
[1] Contributed equally.

https://doi.org/10.1016/j.margeo.2018.11.013
Received 28 June 2018; Received in revised form 3 November 2018; Accepted 18 November 2018
Available online 23 November 2018

venting (Hensen et al., 2003; Haese et al., 2006; Mastalerz et al., 2007, 2009; Mazzini, 2009; Feseker et al., 2010). They generally develop in basins with a thick sedimentary infill. The upward migration of over-pressurized material from deep units is often associated with faults and shale diapirs (e.g., Milkov, 2000). The venting activity in a seepage field is generally heterogeneous in time, space, and strength (Haese et al., 2006; Mazzini, 2009). In the same field of MVs, individual and neighboring structures can have different scales and intensities of fluid discharge, which controls the level of seepage activity and affects the composition of the expelled fluids. In some cases, differences may exist even between individual seep vents inside the crater of a single MV (Mazzini, 2009).

The nature of source strata feeding MVs and the occurrence of sediment-fluid interactions may affect the geochemistry of the expelled fluids and mud (Hensen et al., 2007, 2015). In this regards, the geochemical signature and isotopic composition of the discharged fluids may provide insight into the origin of fluids and the diagenetic processes occurring in the MV system.

In the West Mediterranean, the presently known fluid discharge from MVs is confined to the West Alboran Basin (WAB). This MV field developed in association with a major sedimentary depocentre and under a compressive tectonic regime (Jurado and Comas, 1992; Comas et al., 1999). The present study reports and interprets the geochemical and isotopic composition of pore fluids for sites located at the summit of Carmen MV. We investigate the origin of the fluids and the main diagenetic processes that have affected the fluid composition, integrating pore-water and sediment data. Finally, we run a one-dimensional reaction transport model to constrain fluid provenance and timing of the last eruptive event.

2. Geological background

The Alboran Basin is located in the westernmost part of the Mediterranean Sea (Fig. 1). The major sedimentary depocentre of the basin is in the WAB, consisting of Miocene to Quaternary sedimentary sequences (up to 8 km in thickness) on top of a metamorphic basement (Fig. 2; Comas et al., 1996). The WAB is characterized by widespread shale tectonics (shale diapirism and mud volcanism) conditioned by the existence of deep over-pressurization associated with fluid overpressure in the basal sedimentary units of the WAB (Units VI and Va, from Jurado and Comas, 1992, Fig. 2) and affected by complex tectonic processes (Comas et al., 1999, 2012; Soto et al., 2010).

In the WAB, shale diapirism extends from the Iberian to the Moroccan margin, forming the Mud Diapir Province (MDP; Fig. 1). Within the MDP, MVs develop in association with shale diapirism. Seismic profiles indicate that deep-feeding chimneys of Alboran MVs connect with the oldest and deepest sediments of the basin (Unit VI–Va - Early to Middle Miocene; Jurado and Comas, 1992), with material transported to the surface deriving from overpressured shales (Fig. 2, Talukder et al., 2003; Comas et al., 2012).

Within this region, Carmen MV corresponds to a single edifice with a sub-circular cone shape, 65 m in height and 1 km in diameter at the base (Ivanov et al., 2010). The volcano features gentle slopes of 7° on average, although steeper slopes are observed on the eastern flank with maximum values of 12º (Fig. 3). The central seafloor dome imagery shows very low values of backscattering (Fig. 3a). This fact, together with the seismic chaotic reflection pattern of the feeder channel (Fig. 3b) reveals that recent expulsion of mud-rich fluids has occurred at the summit (Comas et al., 2010; Ivanov et al., 2010; Somoza et al., 2012). Evidence from pore water, mud breccia and chemosynthetic fauna (Blinova et al., 2011; López-Rodríguez et al., 2014 and references therein) indicate that active hydrocarbon (mainly methane) cold seeps occur at Carmen MV, the most active structure in the region. During the retrieval of samples, seepage activity was detected at the box core surface e.g. by hydrogen sulfide smell, the presence of frenulate tubeworms and gas bubbling. An underwater TV-survey from cruise TTR-17 also revealed some free gas bubbling from the seafloor at the central part of the summit (Blinova et al., 2011; Comas et al., 2010; Ivanov et al., 2010).

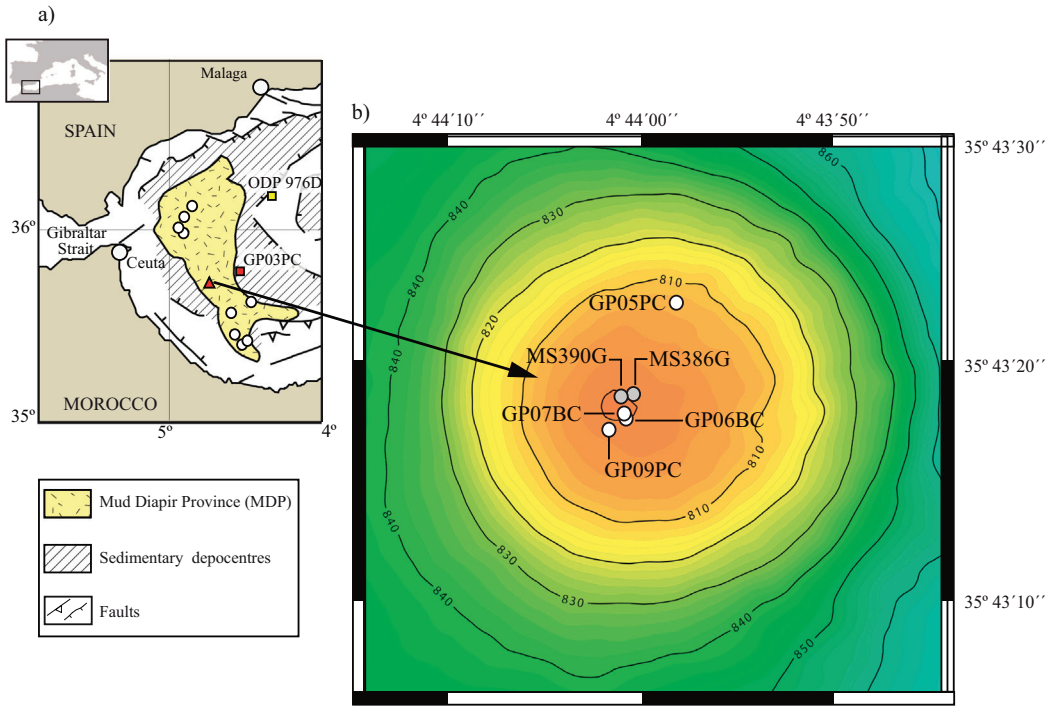

Fig. 1. a) Sketch of the West Alboran Basin (WAB) showing the location of the Mud Diapir Province (MDP). White dots are other reported MVs, whereas red triangle, red square, and yellow square correspond to Carmen MV, core GP03PC, and ODP Leg 161 core-976D respectively. b) Multibeam image of the summit of Carmen MV. White dots belong to the studied cores GP05PC, GP06BC, GP07BC and GP09PC, and grey dots to MS386G and MS390G. (For interpretation of the references to colour in this figure legend, the reader is referred to the web version of this article.)

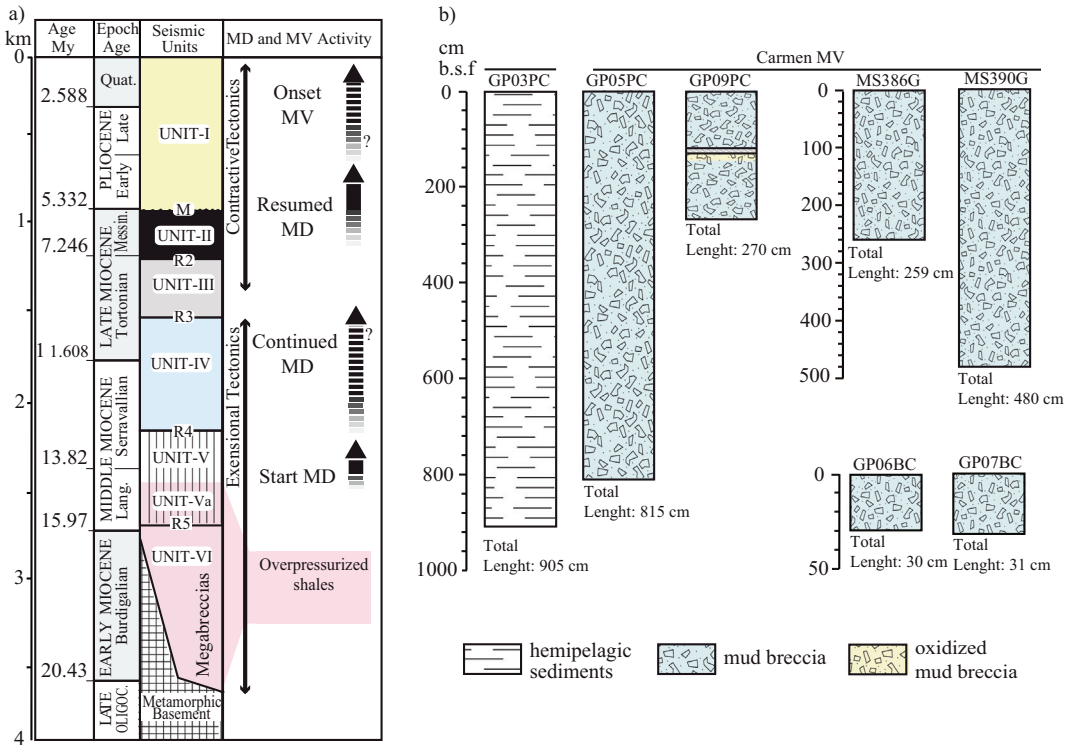

Fig. 2. a) Seismic stratigraphic units, major regional reflectors and main sedimentary sequence (well-log interpretation of the Cenozoic sequence in the Northern Alboran Sea; modified after Jurado and Comas, 1992); M-Messinian unconformity; R-reflectors correspond to major unconformities within sediments; MD refers to mud diapirism; MV corresponds to mud volcanism. b) Schematic core logs showing the main sediment facies from the studied sites. It must be noted that the Alboran sedimentary sequence on top of the metamorphic basement is thought to vary from 4 to 8 km (e.g. Comas et al., 1996), and is likely to be ~5 km at the Carmen MV site.

3. Sampling and analytical procedures

3.1. Multibeam data acquisition and side scan sonographs

Seafloor mapping was done using a high-resolution multibeam Kongsberg EM 302 system during the GASALB Pelagia cruise (*RV* Pelagia, November 2011). The acoustic dataset was obtained with a nominal sonar frequency of 30 kHz, with an angular coverage sector up to 150° and 864 soundings per ping. Multibeam echosounder system data were processed using Kongsberg software to produce a digital terrain model that was mapped and described using morphometric characterization.

3.2. Sediment coring and sampling

The investigated sediment cores were recovered during the GASALB-Pelagia cruise in November 2011 with *RV* Pelagia (NIOZ). In total, three piston-cores and one box-core from the central part of the Alboran MVP were selected for this study (Fig. 1, Table 1). Two piston cores (GP05PC and GP09PC) and one box-core (GP07BC) were taken from the summit of Carmen MV and one piston core was retrieved from a reference site (GP03PC) (Table 1).

Bottom-sampling operations performed during TTR-17 Leg 1 with *RV* Logachev in 2008 used a 6 m long gravity corer (ca. 1500 kg) with an internal diameter of 14.7 cm. The cores were cut in 60 cm sections and after description they were immediately packed and stored at +4 °C for subsequent sub-sampling. Coring on board *RV* Pelagia was performed using a 1200 kg piston corer with maximum tubing 24 m long and with an internal diameter of 11 cm. After recovery, the piston cores were cut into sediment segments of 30 or 50 cm. The round-shaped box corer (ca. 1350 kg) had an internal diameter of 50 cm and a height of 55 cm. Sediments of the box-core were sampled from sub-cores using pvc tubes of 50 cm length and 9 cm inner diameter that were pushed vertically into the sediments.

3.3. Gas extraction and analysis

Samples for gas analyses from piston cores taken during the Pelagia cruise were taken immediately on deck from the top of each freshly cut side of the 30 or 50 cm sections using a 10-ml decapped syringe. Samples from box-cores were taken using predrilled sub-cores, cutting the tape covering the holes and introducing gently a decapped syringe to recover 10 ml of sediment. The 10 ml of fresh sediment sample was immediately transferred into a 65 ml glass vial pre-filled with a saturated NaCl solution. The vials were immediately closed with a thick gas-tight rubber stopper while excluding air, and subsequently well-mixed. After approximate 1 h, 5 ml headspace was made with nitrogen gas (purity 5.0) through the rubber stopper in the upside down bottle while 5 ml of saltwater was simultaneously removed using a second needle. Afterwards, the bottles were shaken again to make a homogeneous suspension and were equilibrated upside down for at least 24 h at room temperature prior to gas analysis (following procedures by Mastalerz et al., 2007). The methane concentration in the headspace was routinely determined on board, injecting 1 ml gas sample into a Shimadzu Gas Chromatograph GC-14B with a flame ionization detector and equipped with a packed stainless steel Porapack Q (6 ft, 2 mm i.d., 80/100 mesh, Alltech).

The isotopic signature of methane was measured with continuous flow isotope ratio mass spectrometry systems at the Institute for Marine and Atmospheric Research (IMAU), Utrecht (The Netherlands) for $\delta D_{methane}$ and at the Royal Holloway University of London (RHUL), London (United Kingdom) for $\delta^{13}C_{methane}$.

Subsamples were extracted from the headspace present in the sealed flasks and injected to the sample loop of each system to be mixed with a

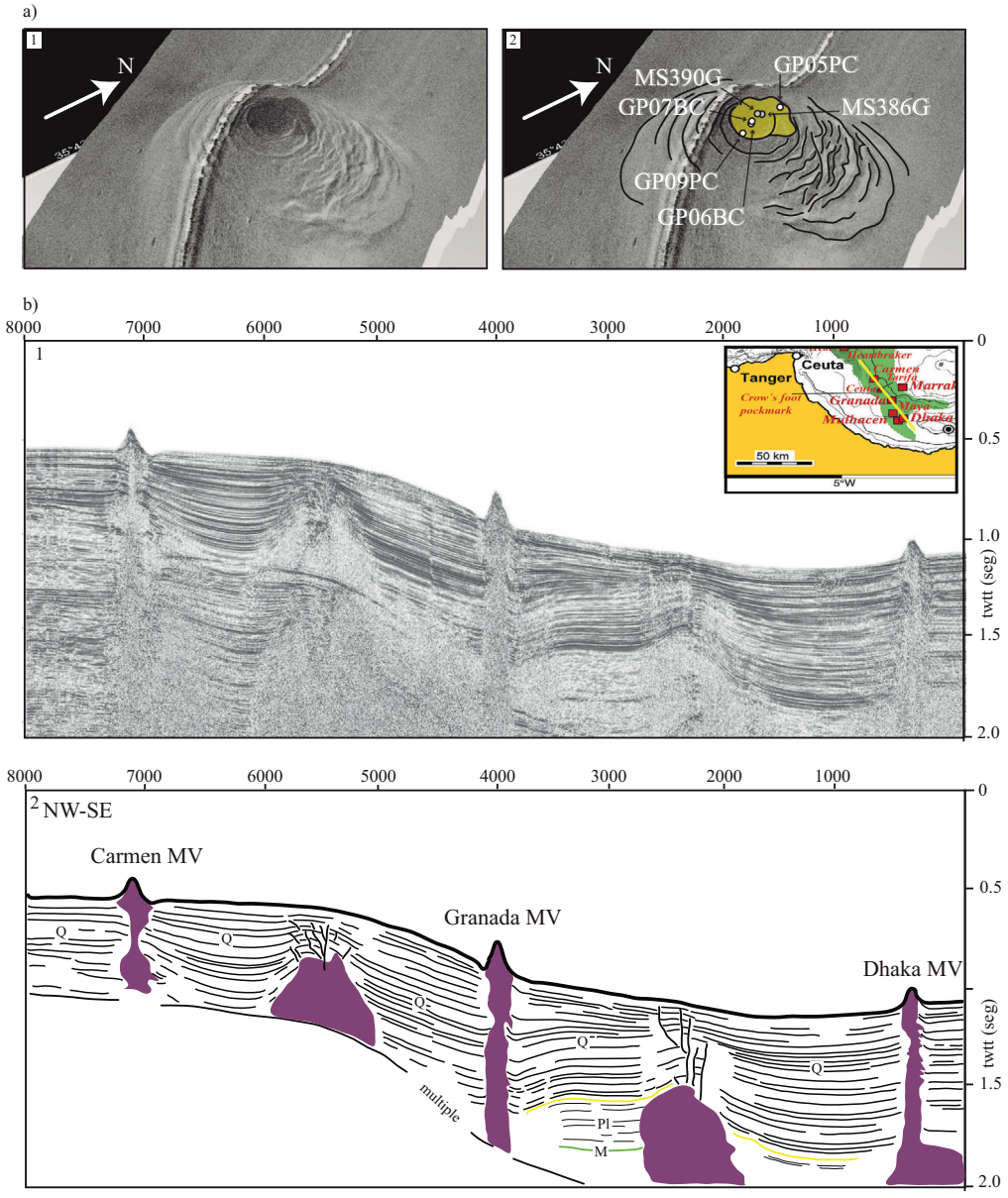

Fig. 3. a) MAK 1 sonograph from Carmen MV (100 KHz sidescan sonar; Ivanov et al., 2010) un-interpreted (1) and interpreted (2) showing the cone-shaped morphology, concentric mud flows and the location of the studied cores. Yellow coloured area (2) corresponds to low backscatter, indicating a recent mud flow. b) Un-interpreted (1) and interpreted (2) high resolution seismic profile across Carmen, Granada and Dhaka MVs (Comas et al., 2010). Purple coloured areas indicate feeding channels from overpressured shales and megabreccias. The yellow line refers to seismic reflectors within the Plio-Quaternary sequence (Unit I) whereas the green line refers to the Messinian unconformity (Comas et al., 2010). (For interpretation of the references to colour in this figure legend, the reader is referred to the web version of this article.)

carrier gas (Helium). High precision measurements of $\delta D_{methane}$ and $\delta^{13}C_{methane}$ were obtained by sample pre-concentration, cryofocusing and subsequent pyrolysis to H_2 or combustion to CO_2 for measurement of either stable isotope, before entering the mass spectrometers: a Trace Gas and Isoprime mass spectrometer (Isoprime Ltd) for $\delta^{13}C_{methane}$ (Fisher et al., 2006) and a ThermoFinnigan MAT Deltaplus XL for $\delta D_{methane}$ (Brass and Röckmann, 2010; Sapart et al., 2011).

Table 1
General information about sampling and positioning of the studied cores.

Core code	Site	Cruise	Location	Sampling Site	Water[b] depth (m)	Recovery (cm)
976D	Hemipelagic	ODP Leg 161	36° 12.330′ N 04° 18.744′ W	Hemipelagic	1108	3100[a]
GP03PC	Hemipelagic	GASALB-Pelagia	35° 47.261′ N 04° 32.089′ W	Hemipelagic	1306	905
GP05PC	Carmen MV	GASALB-Pelagia	35° 43.370′ N 04° 43.970′ W	MV-summit	802	815
GP06BC	Carmen MV	GASALB-Pelagia	35° 43.290′ N 04° 44.028′ W	MV-summit	798	30
GP07BC	Carmen MV	GASALB-Pelagia	35° 43.299′ N 04° 44.016′ W	MV-summit	798	31
GP09PC	Carmen MV	GASALB-Pelagia	35° 43.286′ N 04° 44.030′ W	MV-summit	798	270
MS386G	Carmen MV	TTR-17	35° 43.309′ N 04° 44.008′ W	MV-summit	809	259
MS390G	Carmen MV	TTR-17	35° 43.306′ N 04° 44.017′ W	MV-summit	809	250

[a] Interval reported here.
[b] GASALB-Pelagia water depths corrected based on acoustic observations. The GASALB-Pelagia acoustic-derived depths were corrected using GP08CT station CTD-data and altimeter-derived few-m distance to bottom. The bottom-depth derived for this station, taken between GP05PC and GP07BC was 799.9 m for CTD-data and 794.7 m for acoustic data. Hence a correction factor of 1.0065 was applied to all Carmen MV stations.

3.4. Pore-water extraction

Samples for the extraction of pore water from piston-core sediments were taken directly on deck from the cut sides of each section. The two cut-off 60 ml syringes were pushed into the bottom of each 30 or 50 cm section of the piston core, and the recovered sediment was transferred into 50 ml plastic centrifuge tubes with screw caps. These were centrifuged for 15–60 min at 2800–3500 rpm in a cooled laboratory at the in situ temperature of +14 °C (De Lange, 1992a).

Further pore-water extractions were carried out on these sections while being stored at +14 °C. This was done in an on-board laboratory, maintained at in-situ temperature, using rhizons (Seeberg-Elverfeldt et al., 2005) pushed into the top of each 30 or 50 cm piston-core section. For water-saturated sediment samples, rhizons were left with reduced pressure for at least 30 min, whereas for relatively dry samples, rhizons remained operational overnight. For the box-core, pore-water extractions were done at high resolution pushing rhizons into the sediment every 2 cm through pre-drilled holes in the pvc tube. After extraction, all aliquots were filtered and subsampled for onboard analyses and/or stored at +4 °C.

For piston core GP05PC, the mud breccia intervals except for the uppermost part had low water content, and little pore water was recovered using centrifugation. Additional pore water was extracted from these centrifuged sediments by pushing the rhizons into the sediment within the centrifuge tubes. After centrifugation or rhizon extraction, the pore waters were transferred into an anoxic glove-box under a N_2-atmosphere, where it was filtered through 0.2 µm cellulose-acetate membrane filters. Samples were subsequently split into sub-samples for shipboard analyses or stored at +4 °C prior to shore-based pore-water analyses. For many samples the pore-water recovery was too small to permit subsamples for all analyses.

After sampling for gas and pore water, all sediment sections were stored at +4 °C for future on-land analyses.

3.5. Pore-water analyses

After pore-water extraction and filtration, the most sensitive parameters were measured on board. Thus, total alkalinity (TA) was determined by titration with HCl following the procedure of Grasshoff et al. (1983). Dissolved inorganic carbon (DIC) was analyzed spectrophotometrically using a continuous flow set-up (Stoll et al., 2001). Concentrations of sulfide (HS^-) were also determined immediately, using standard photometric procedures adapted for pore waters with relatively high concentrations (~mM) of dissolved sulfide. For ammonia (NH_4^+) and phosphates (PO_4^{3-}), all analyses were carried out on board with a continuous flow analyzer, applying auto-analyzer colorimetric methods (after Grasshoff et al., 1983).

Total dissolved anions (Cl^-, SO_4^{2-} and Br^-), cations (Na^+, Ca^{2+}, Mg^{2+}, K^+, Ba^{2+}, Li^+, Sr^{2+}) and H_3BO_3 (boric acid) concentrations in the pore-water samples were measured by means of an inductively coupled plasma atomic emission spectrometer (ICP-AES, Perkin Elmer Optima 3000) and an inductively coupled plasma mass spectrometer (ICP-MS, ThermoFisher Scientific Element2-XR) in the shore-based laboratory at the Department of Earth Sciences of Utrecht University, Utrecht (The Netherlands). The ICP-MS measurements had a relative error < 3%. Accuracy and precision of the ICP-AES analyses were established by measuring laboratory reference material and sample replicates; relative errors were < 5% for all reported elements.

Total dissolved solids (TDS) were calculated from the sum of dissolved species in the porewater as determined by ICP-AES. Mediterranean seawater of 37.976 salinity, recovered at CTD station GP08CT immediately above Carmen MV was analyzed in the same series (n = 10), and resulted in a TDS value of 38.0 ± 0.3 g/kg.

The stable carbon isotope values of DIC ($\delta^{13}C_{DIC}$) in pore waters were obtained by means of elemental analyzer-continuous flow isotope ratio-mass spectrometry using a Fisons 1500 NCS elemental analyzer coupled to a Finnigan Mat Delta Plus mass spectrometer. The accuracy of the internal standards was ± 0.06‰. The $\delta^{13}C_{DIC}$ was reported in standard delta notation (‰) relative to the VPDB standard. Average analytical precision based on routine analysis of internal laboratory reference material demonstrated a standard deviation of 0.15‰.

Stable oxygen ($\delta^{18}O_{pw}$) and hydrogen (δD_{pw}) isotope values of pore waters were determined using the H_2O–CO_2 and H2O-H2 equilibration method (Nelson, 2000) and continuous flow technology with a helium carrier gas, performed in a GasBench II coupled to a Thermo Delta-V mass spectrometer. The accuracy of the internal standards was ± 0.1‰ for $\delta^{18}O_{pw}$ and ± 1‰ for δD_{pw}. Average analytical precision based on routine analysis of internal laboratory reference material demonstrated standard deviations of 0.1 and 3‰, respectively. The $\delta^{18}O_{pw}$ and δD_{pw} of pore water were reported using the standard delta notation (‰) relative to the V-SMOW standard.

Radiogenic strontium isotopes were measured by MC-ICP-MS (Thermo Scientific Neptune Plus multi-collector ICP-MS) after chromatographic strontium separation using Sr-Spec resin (©Eichrom) at the Institute for Chemistry and Biology of the Marine Environment (ICBM), University of Oldenburg (Germany).

Chemical separation of Sr and analyses of $^{87}Sr/^{86}Sr$ isotope ratios were examined by repeated analyses of the Strontium Carbonate isotopic standard SRM 987 from the NIST (National Institute of Standards and Technology) and IAPSO seawater standard; the average of the external reproducibility of the NIST SRM 987 is ± 4.5E−06 (2σ, n = 16). Sr-isotope ratios were normalized to the NIST SRM 987 standard (0.710248; Howarth and McArthur, 1997).

3.6. Mineralogical analyses and smectite to illite transformation determinations

Samples for mineralogical analyses were taken from the mud breccia intervals every 5 or 10 cm at 2 cm thick intervals while avoiding rock fragments. Samples were dried in an oven at 40 °C; ground and homogenized in an agate mortar.

Analyzed samples correspond to piston core GP05PC and gravity cores MS386G and MS390G. Bulk and clay-mineral composition was determined by X-ray diffraction (XRD) at the Andalusian Earth Sciences Institute (CSIC-University of Granada, Spain). Separation of the < 2 µm fraction and preparation of samples for XRD analyses were performed following Moore and Reynolds (1997). X-ray diffractograms were obtained using a PANalytical X'Pert PRO diffractometer equipped with an X'Celerator solid-state linear detector, using a step increment of 0.01° 2θ and a counting time of 1 s/step, with Cu-Kα radiation (45 kV, 40 mA) and an automatic slit. Scans were run from 3 to 50° for untreated clay preparation as well as for glycolated samples. Resulting diffractograms were interpreted using XPowder software (Martin-Ramos, 2006. www.xpowder.com).

Clay-mineral transformation was confirmed by deconvolution. The illite-smectite mixed-layers minerals (I/S) were analyzed using *MacDiff* 4.2.5 software (Petschick, 2004). The peak near 14 Å was used to differentiate expandable mixed-layer minerals, such as smectite or R0 illite/smectite mixed-layers, which expand to 15–17 Å after ethylene glycol saturation. The determination of the percentage of illite (% I) was performed by deconvolution of XRD peaks 001/002 and 002/003 for the regions 10.3–9.0° 2θ and 15.8–17.4° 2θ respectively (Moore and Reynolds, 1997; Nieto et al., 2016). XRD patterns of the glycolated samples showed the simultaneous occurrence of disordered R0 and ordered R1–R3 I/S in all the studied mud breccia matrices (Fig. 4).

3.7. Geochemical modeling

A one-dimensional reaction transport model (e.g. Boudreau, 1997; Mogollón et al., 2012) consisting of 8 species (Table 2) and 4 reactions was used to simulate the sediment geochemistry at Carmen MV. The model couples reactions through a discretized reaction-transport

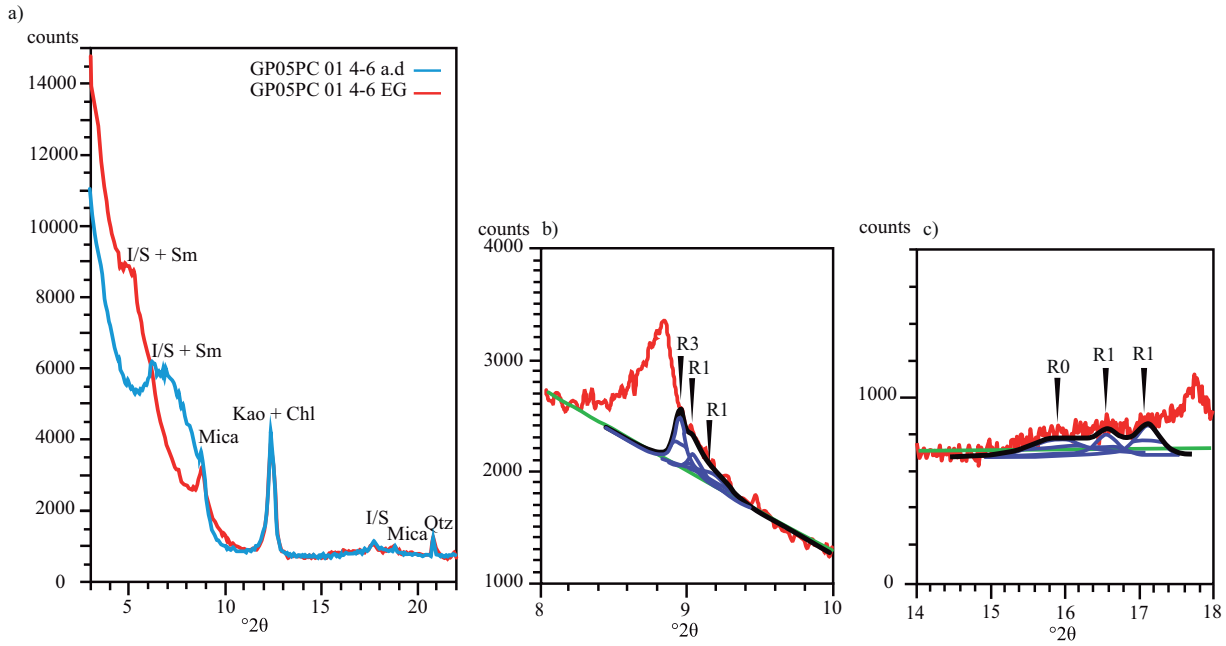

Fig. 4. Example of a) Air-dried and ethylene glycol-solvated XRD patterns of a < 2 μm fraction for a mud breccia matrix sample studied from core GP05PC. Mica refers to illite and possible other micas of detrital origin; b–c) decomposition of XRD peaks 001/002 and 002/003 on the regions b) 10.3–9.0° 2θ and c) 15.8–17.4° 2θ (using *MacDiff* 4.2.5). R0–R3 are based according to Moore and Reynolds (1997).

equation (Eq. (1)):

$$\vartheta_i \frac{\partial C_{i,j}}{\partial t} = \frac{\partial D_{i,j} \vartheta_i \left(\partial C_{i,j}/\partial z\right)}{\partial z} - \frac{\partial \omega_i \vartheta_i C_{i,j}}{\partial z} + \vartheta_i \sum R_i \quad (1)$$

where t is time, z is sediment depth, and i, j represent subscripts depicting depth- and species-dependence respectively. C is the species concentration (aqueous or solid species, Table 2); D is the diffusive mixing coefficient taking tortuosity into account (Boudreau, 1997); ϑ is the volume fraction for the aqueous (i.e. the porosity φ_i) or solid ($1 - \varphi_i$) phases; ω_i is the velocity of either the aqueous or the solid phase (v_i or w_i, respectively); ΣR_i is the sum of the reactions affecting the given species j. The first term of the right hand side of Eq. (1) represents diffusion, the second term represents advection, and the final term represents the reactions affecting species j. Bioturbation and bioirrigation were assumed to be of minor importance and thus ignored from the simulations. Four reactions were taken into account in the model (species in **bold** are explicitly modeled, with CO_3^{2-} and HCO_3^- modeled in combination as DIC):

Organoclastic sulfate reduction ($\mathbf{CH_2O} + 1/2\ \mathbf{SO_4^{2-}} + H_2O \rightarrow 1/2\ HS^- + HCO_3^- + 1/2\ H^+$) was quantified assuming a reactive continuum (Boudreau and Ruddick, 1991):

$$R_{SR} = \frac{\sigma}{a} \frac{(C_{CH2O})^{1+1/\sigma}}{(C_{0,CH2O})^{1/\sigma}} \frac{C_{SO4}}{C_{SO4} + K_{SO4}} \quad (2)$$

where σ, a are parameters related to a gamma function distribution to describe the organic matter degradation profile (see Boudreau and Ruddick, 1991 for further details), and K_{SO4} is an inhibition constant for methanogenesis under the presence of sulfate.

Methanogenesis ($\mathbf{CH_2O} + 1/2\ H_2O \rightarrow 1/2\ \mathbf{CH_4} + 1/2\ \mathbf{HCO_3^-} + 1/2\ H^+$) was quantified also assuming a reactive continuum with an inhibition based on the presence of sulfate:

$$R_{MET} = \frac{\sigma}{a} \frac{(C_{CH2O})^{1+\frac{1}{\sigma}}}{(C_{0,CH2O})^{\frac{1}{\sigma}}} \frac{K_{SO4}}{C_{SO4} + K_{SO4}} \quad (3)$$

Anaerobic oxidation of methane ($\mathbf{CH_4} + \mathbf{SO_4^{2-}} \rightarrow HS^- + \mathbf{HCO_3^-} + H_2O$) was quantified assuming bimolecular kinetics:

$$R_{AOM} = k_{AOM} C_{SO4} C_{CH4} \quad (4)$$

where k_{AOM} is a rate constant for anaerobic oxidation of methane (AOM).

Calcite precipitation ($\mathbf{CO_3^{2-}} + \mathbf{Ca^{2+}} \rightarrow CaCO_3$):

Table 2
Modeled species, boundary conditions[a] (B.C.) and reactions.

Species	Species unit	Top boundary condition type[b]: unit	Top B.C. value	Reaction rate	Initial condition (profile after mudflow event)
TOC	dry wt%	F: mol $m^{-2} y^{-1}$	0.052	$-R_{SR} - R_{MET}$	Steady-state solution
SO_4^{2-}	mM	C: mM	33	$-0.5\ R_{SR} - R_{AOM}$	33 exp((230 − z) / 0.5) / (1 + exp((230 − z) / 0.5))
CH_4	mM	C: mM	0	$0.5\ R_{MET} - R_{AOM}$	35 + (0.1–35) exp((184 − z) / 0.5) / (1 + exp((184 − z) / 0.5))
Ca^{2+}	mM	C: mM	13	$-R_{Cal}$	13 exp((230 − z) / 0.5) / (1 + exp((230 − z) / 0.5))
Cl^-	mM	C: mM	640	0	180 + (640–180) exp((230 − z) / 0.5) / (1 + exp((230 − z) / 0.5))
NH_4^{2+}	mM	C: μM	1	$r_{N:C}(R_{MET} + R_{SR})$	1300 + (1−1300) exp((230 − z) / 0.5) / (1 + exp((230 − z) / 0.5))
PO_4^{3-}	mM	C: μM	0.8	$r_{P:C}(R_{MET} + R_{SR})$	2 + (0.8–2) exp((230 − z) / 0.5) / (1 + exp((230 − z) / 0.5))
DIC[c]	mM	C: mM	3.5	$R_{SR} + 0.5\ R_{MET} - R_{Cal}$	38 + (3.5–38) exp((230 − z) / 0.5) / (1 + exp((230 − z) / 0.5))

z = sediment depth (in cm).
[a] Bottom boundary was zero gradient for all species.
[b] F = Fixed flux, C = Fixed concentration.
[c] DIC = $CO_3^{2-} + HCO_3^-$.

Table 3
Model parameters[a].

Symbol	Value	Unit
ϕ	0.55[b]	–
ϕ	0.5[b]	–
β	0.001[b]	cm^{-1}
v	10	$cm\,ky^{-1}$
T	279	K
S	37	–
σ	0.125	–
a	8000	y
pH	7.5	–
k_{AOM}	5.0	$mmol^{-1}\,l\,y^{-1}$
k_{Cal}	10.0	$mM\,y^{-1}$
$r_{N:C}$	16/106	–
$r_{P:C}$	1/106	–
K_{SO4}	1.6	mM

[a] All values are assumed for this study.
[b] Porosity is calculated as an exponentially decreasing function with depth (z): $\phi_z = \phi_{inf} + (\phi_0 - \phi_{inf})e^{-\beta z}$.

$$R_{Cal} = k_{Cal}(1-\Omega)^2,\ \Omega > 1$$
$$R_{Cal} = 0,\quad \Omega \le 1 \tag{5}$$

where k_{Cal} is a rate constant for calcite precipitation. The saturation index (Ω) was calculated as the multiplication of the molar concentrations of carbonate and calcium ions over the solubility product (K_{sp}):

$$\Omega = \frac{C_{Ca}\left(\frac{C_{DIC}K_2}{10^{-pH}+K_2}\right)}{K_{sp}} \tag{6}$$

where the term in parenthesis is the carbonate concentration calculated from DIC. K_{sp} and K_2 were calculated after Lueker et al. (2000).

The model was coded in R (version 3.2.4) using the *ReacTran* (Soetaert and Meysman, 2012) and *marelac* (Soetaert et al., 2010) packages, with the former solving the differential equations and the latter solving for the diffusion coefficients. Burial rates were assumed to be similar to modern shelf settings. All parameters used in the simulations are stated in Table 2.

All simulated parameters used for the reaction model are listed in Tables 2 and 3 and shown at Fig. 5. The numerical model simulates transient states, assuming a hypothetical initial situation without sulfate diffusion and no methane upward migration (t = 0). Step gradients between the uppermost unit with typical seawater-like signature and the lower unit with deep-fluid composition develop on a time scale of years and decades (Fig. 6).

3.8. Statistics used

For the comparison between measured and simulated geochemical species, we used root mean square error (*RMSE*, Eq. (7)):

$$RSME = \sqrt{\frac{\sum_{i=1}^{n}((S_i - M_i)^2)}{n}} \tag{7}$$

where S_i is the simulated value, M_i is the measured value and n is the number of data pairs. The *RMSE* estimates the average deviation between simulations and measurements. It is an unbounded measure which shows the relative size of the average difference. We select the age when we achieve the minimum RMSE for each biogeochemical species. We then average these ages and take the standard deviation to obtain 12 ± 5 yrs.

4. Results

4.1. Core lithology

Box-cores GP06BC and GP07BC recovered 30 and 31 cm, respectively, of typical structureless dark-grey mousse-like mud breccia with a clear degassing texture (Fig. 2; and Table 1). At box-core GP07BC, the surface veneer (probably < 0.1 mm thick) was brownish thus oxidized, whereas some methane bubbling was discernible, as well as the presence of *Pogonophora* tubeworms. Chemosynthetic fauna such as live *Acharax* shells and white crabs were found.

Piston core GP05PC recovered 815 cm of typical structureless and dark-greyish mousse-like mud breccia (Fig. 2), with millimeter-to centimeter-sized rock clasts of claystones and mudstones. At this site, no hemipelagic sediments were present and a noticeable smell of H_2S was detected along the whole core.

Piston core GP09PC recovered 270 cm, containing two distinct mud breccia intervals, separated by a thin interval of hemipelagic sediment. The uppermost mud breccia interval consisted of soft dark-grey mousse-like mud breccia, highly porous due to degassing processes. A strong smell of H_2S was noted at this interval, and *Pogonophora* tubeworms were present. Additionally, an authigenic carbonate crust was found at ca. 10 cm depth. From 120 to 131 cm the interlayered hemipelagic sediment consisted of yellowish-olive grey marls with low content in foraminifera. This layer had a sharp upper boundary whereas the lower limit was irregular and not well-expressed. The lower mud breccia interval extended from 132 to the core bottom at 270 cm. A slightly discoloured, potentially oxidized interval was observed in its uppermost part, extending from 132 to 145 cm. Downcore, relatively stiff and laminated dark-grey mud breccia occurred (Fig. 2).

Gravity cores MS386G and MS390G recovered 259 cm and 480 cm respectively, and consisted both of greenish-grey mousse-like mud breccia (Fig. 2). *Pogonophora* tubeworms were observed in the upper centimetres of core MS386G. No hemipelagic marls were encountered and a strong smell of H_2S was detected at these sites.

Piston core GP03PC was taken off the MV structure. It consisted of 905 cm of olive-grey marls, homogeneous and structureless, without any evidence of mud breccia or MV-derived material (Fig. 2).

Published results from ODP Leg 161 core-976D are used as reference for the pore-water composition (Comas et al., 1996).

4.2. Mineral composition of mud breccia matrix

Clay mineral assemblages of mud breccia matrices showed predominance of mica-illite, smectite, and illite-smectite interstratified minerals (I/S; Fig. 4). Minor amounts of other clay minerals such as kaolinite and chlorite were also identified. The XRD patterns of the glycolated samples showed the occurrence of ordered R0–R3 I/S mixed layers with a percentage of illite ranging between 20 and > 90% for core GP05PC (Table 4).

4.3. Fluid composition

4.3.1. Dissolved major and trace elements

Pore waters from hemipelagic core GP03PC, off the MV structures, have SO_4^{2-} concentrations decreasing gradually from typical bottom water values of 29.5 to 6.4 mM at 868 cm depth in the sediment. Total Alkalinity (TA), dissolved inorganic carbon (DIC), NH_4^+ and PO_4^{3-} concentrations increased gradually with depth (Fig. 7, and Supplementary material-Fig. S1). Salinity and related dissolved constituents and ratios (e.g. Cl^- and Na/Cl ratio) showed constant values with depth. The same is observed for B/Cl, Li/Cl, Ba/Cl and Br/Cl ratios (Fig. 8). In contrast, Ca/Cl, Sr/Cl, K/Cl and Mg/Cl ratios gradually decreased with depth.

The analyzed pore waters of the different mud breccia cores from Carmen MV display geochemical patterns that are very different from

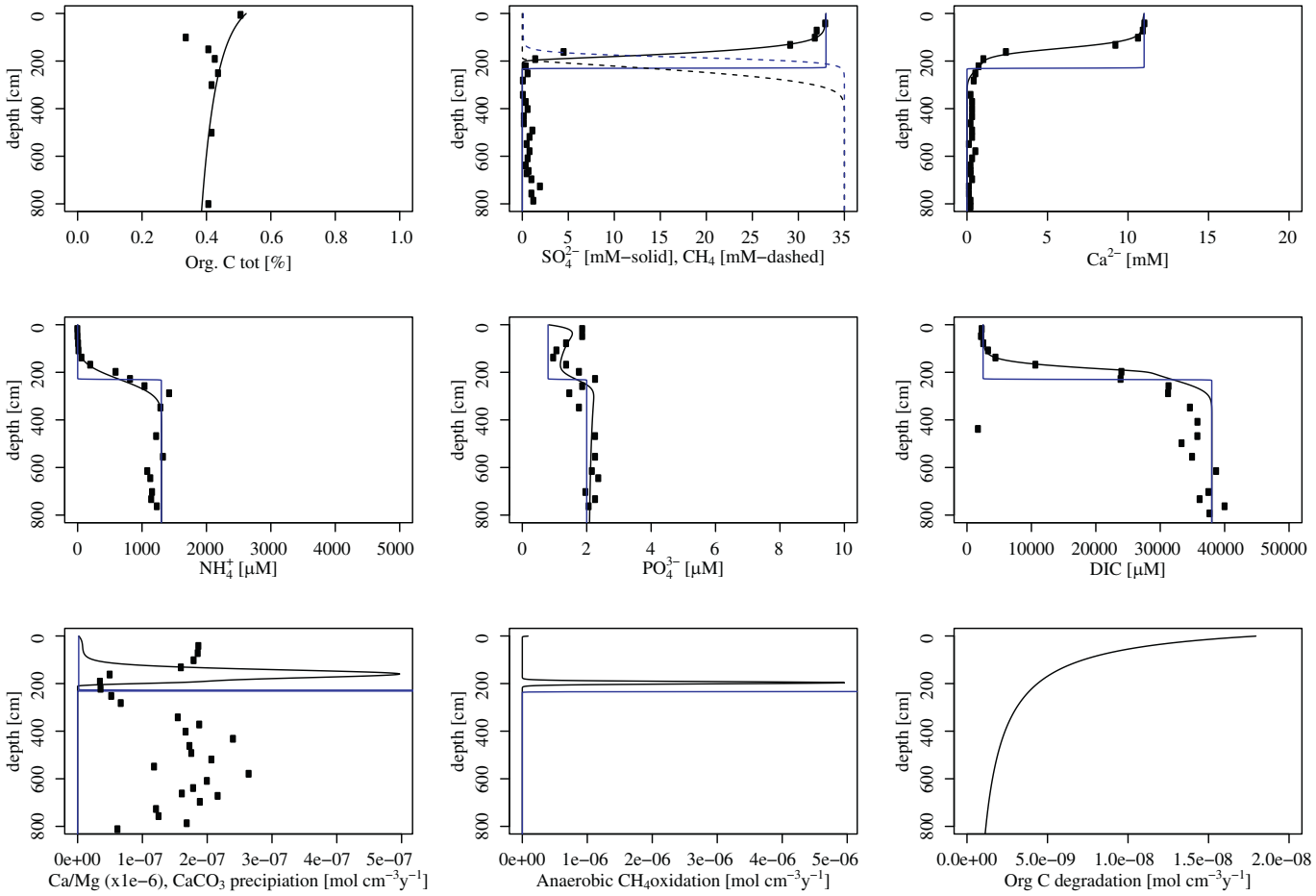

Fig. 5. Numerical modeling profiles for organic carbon, sulfate and methane, calcium, ammonium, phosphate, dissolved inorganic carbon (DIC), (Ca/Mg), and calcite precipitation rates, anaerobic oxidation of methane (AOM) rates, and organic carbon degradation rates. Blue lines indicate time just after the ceasing of the fluid expulsion from the sediment. Black lines indicate the time after 12 years. Open circles indicate the measured data. (For interpretation of the references to colour in this figure legend, the reader is referred to the web version of this article.)

those in hemipelagic cores GP03PC and ODP Leg 161 core-976D (Figs. 7 and 8). The lowermost pore waters from Carmen MV mud breccias were strongly depleted in Cl^- and Na^+, varying from local bottom seawater values of ~613 mmol/kg Cl^- and ~515 mmol/kg Na^+ in the uppermost sediments to minimum concentrations of ~170 mmol/kg and ~200 mmol/kg, at depth. Correspondingly, the salinity significantly decreased from seawater values to low-salinity values at depth, as illustrated by the amount of total dissolved solids (Table 5). To emphasize if changes are due to reduced salinity or other processes, it is common to express elements as the elemental ratio relative to a Cl^-. At the surface, the Na/Cl ratio was similar to that in the bottom water (0.86). However, in the deepest sediments this ratio increased to as much as 1.15 (Fig. 8). Deep fluids were strongly depleted in Ca/Cl, Mg/Cl and K/Cl ratios and considerably enriched in Sr/Cl, B/Cl, Li/Cl, Ba/Cl, and Br/Cl ratios (Fig. 8).

The porewater SO_4^{2-}/Cl ratio decreased to zero below 20 cm sediment depth in core GP07BC and below 220 cm sediment depth in core GP05PC (Fig. 7). From this depth downward, an increase in the concentration of CH_4 to maximum values of 1526 µM was detected (core GP05PC; Fig. 7). The topmost sediment from box-core GP06BC had CH_4 concentrations of 343 µM. TA and DIC run parallel, increasing with depth to values of 42.2 meq/l and 40.2 mM, respectively in core GP05PC. Strong enrichments in NH_4^+ and PO_4^{3-} concentrations were detected at depth for all sites. In GP05PC, HS^- increased significantly between 78 and 228 cm, reaching maximum values of 917 µM (Fig. 7).

4.3.2. Isotopes ($\delta^{13}C_{DIC}$, δD_{pw}, $\delta^{18}O_{pw}$) and $^{87}Sr/^{86}Sr$ ratios

Pore waters from core GP05PC showed δD_{pw} values ranging from +12 to −10‰, with a general decreasing trend versus depth. In contrast, the $\delta^{18}O_{pw}$ values increased down core, ranging from +1.0 to +5.7‰ (Fig. 9). The $\delta^{13}C_{DIC}$ from the investigated pore fluids varied from −8.5‰ in the uppermost mud-breccia interval to −20.8‰ at 167.5 cm, the lowermost sample for which we had enough material for this analysis (Fig. 9 and Table 6).

Two deep pore-water samples of GP05PC were analyzed for radiogenic strontium isotopes. The isotopic values showed similar $^{87}Sr/^{86}Sr$ ratios for both samples with an average value of 0.70901 ± 0.00002 (Table 6).

The stable carbon and hydrogen composition of methane were analyzed for cores GP05PC, GP07BC and GP09PC. The $\delta^{13}C_{methane}$ results revealed depleted values for all three sites: −69.8‰ to −59.0‰ VPDB in GP05PC, −42.3‰ to −31.3‰ VPDB in GP07BC; and −58.7 to −58.0‰ VPDB in GP09PC. The $\delta D_{methane}$ data are also depleted, being −184‰ to −88‰ VSMOW in GP05PC, −65‰ to −53‰ VSMOW in GP07BC and −181‰ to −180‰ VSMOW in GP09PC (Fig. 7).

5. Discussion

The pore-water composition of core GP09PC taken at Carmen MV closely reflects the observed alternating mudflows and interbedded fine-grained hemipelagic interval (Figs. 2, 7 and 8). In contrast, the absence of hemipelagic draping and hemipelagic intervals in core

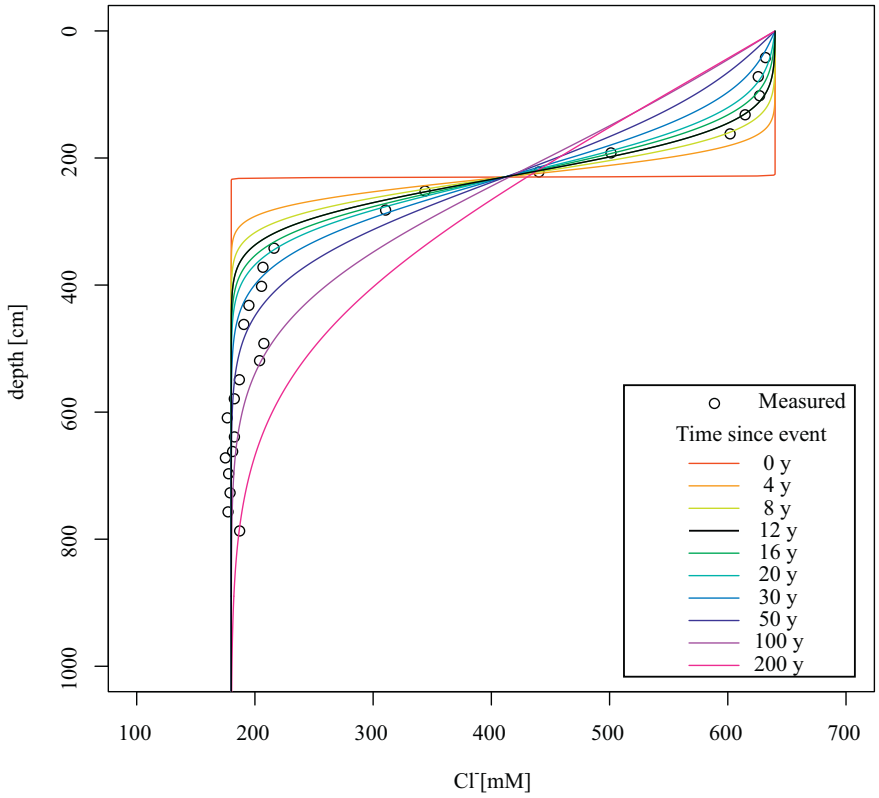

Fig. 6. Numerical modeling profiles of dissolved chloride (Cl^-) for different timings of the eruptive event in GP05PC. Circles indicate Cl^- measured data. The best-fit is obtained for 12 ± 5 yrs.

Table 4
Positions (Cu kα) of detected reflections and estimating percent of illite layer in illite/EG-smectite from selected mud breccia sample from GP05PC from Carmen MV. R denotes the Reichweite number.

% illite	R	001/002		002/003		
		d(Å)	2θ	d(Å)	2θ	Δ2θ
Carmen MV GP05PC						
20	0	–	–	5.57	15.89	–
60	1	–	–	5.35	16.58	–
80	1	9.64	9.17	–	–	–
85	1	9.77	9.04	5.18	17.11	8.07
> 90	3	9.86	8.96	–	–	–

GP05PC, also taken at the summit of Carmen MV, point to rapid depositional processes and accumulation of mud breccia, evidencing active mud expulsion (e.g. Hensen et al., 2007; Mastalerz et al., 2007; Ivanov et al., 2010). The abrupt transition that occurs between high- and constant dissolved sulfate content in the uppermost interval and low sulfate together with high methane concentrations in the lowermost sediment interval (particularly in cores GP05PC and GP07BC, Figs. 7 and 8), emphasizes the high rate and recent occurrence of such process.

5.1. Seawater-like pore-water composition of the uppermost interval of mud breccia

Sediments from active zones of MVs usually have characteristic pore-water concentration profiles (i.e., SO_4^{2-}, CH_4) that reflect upward fluid advection of methane and the occurrence of sulfate-reduction processes (Hensen et al., 2007 and references therein). The shapes of pore-water profiles, especially those of decreasing sulfate with increasing sediment depth, provide information about the geochemical condition of the system and interactions among dissolved species, in particular between sulfate and methane. Nevertheless, the anomalous seawater-like pore-water composition recently encountered at summits and active parts of MVs (i.e., Mastalerz et al., 2007; Feseker et al., 2010; Reitz et al., 2011) suggests that sedimentary events or eruptive episodes of mud expulsion may adversely affect the composition of pore fluids in the uppermost part of the mud breccia interval (Hensen et al., 2007; Mastalerz et al., 2007; Feseker et al., 2010; Reitz et al., 2011).

Correspondingly, our pore-water profiles reveal a distribution versus depth that is remarkable. This is especially evident for the Carmen MV summit mud-breccia cores, where sulfate remains at seawater concentration for the uppermost 25 cm in box-core GP07BC and for the uppermost 130 cm in piston core GP05PC (Figs. 7 and 8). This constant pore-water composition differs significantly from that observed in core GP03PC taken outside of the MDP and in reference core ODP Leg 161 core-976D (both: hemipelagic sediments, Figs. 1, 7 and 8). The sulfate concentration in GP03PC and ODP Leg 161 core-976D, decreasing from the topmost sediment downward (Fig. 7), indicates ongoing sulfate-reducing processes, likely to be associated with organic matter (OM) degradation. The latter is consistent with the observed increase in associated biogenic components in the pore water of these cores.

In the uppermost MV sediments, not only does the concentration of sulfate remain constant at bottom-water level but the concentrations of OM-degradation related products (e.g., NH_4^+, PO_4^{3-}, TA, and DIC; Fig. 7) remain low and nearly constant. The absence of substantial OM-degradation in the uppermost interval of MV-mud-breccia is in contrast to the clear OM-degradation processes observed in the reference hemipelagic ODP Leg 161 core-976D and core GP03PC. In addition, the pore-water δD_{pw} and $\delta^{18}O_{pw}$ reflect a typical seawater composition for these upper intervals (Fig. 9).

Hence, for the Carmen MV summit cores GP07BC and GP05PC, the pore water of the uppermost interval clearly has a seawater-like

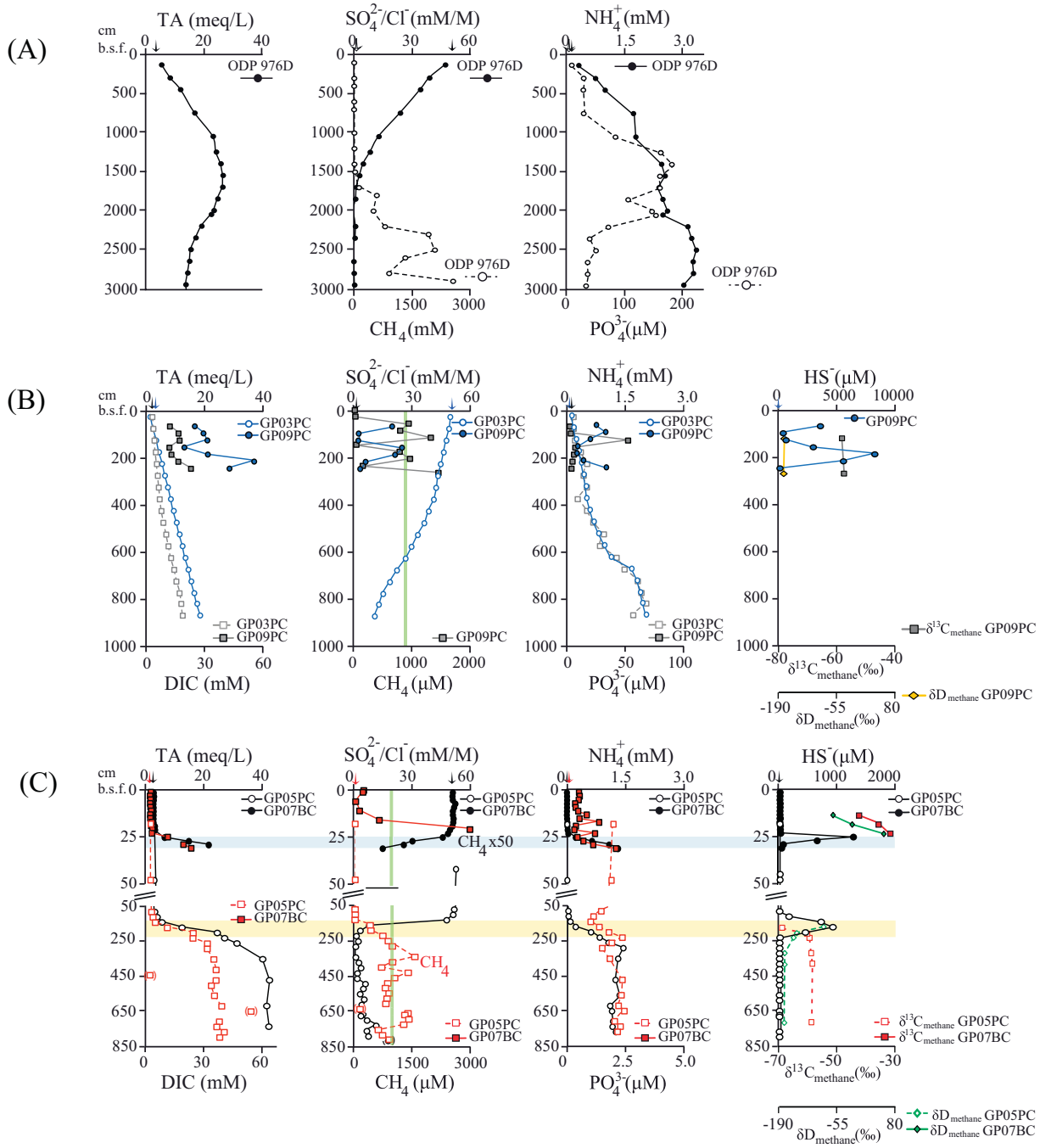

Fig. 7. Pore-water profiles of the concentration versus depth for: Total Alkalinity (TA), dissolved inorganic carbon (DIC), SO_4^{2-}/Cl^-, NH_4^+, PO_4^{3-}, HS^-, and methane (CH_4); and the stable carbon and hydrogen isotope composition of methane versus depth, for ODP Leg 161 core-976D and GP03PC (hemipelagic sediments), GP09PC (alternating hemipelagic and mud breccia units), GP05PC and GP07BC (fully mud breccia). Values are expressed in mM/l and µM/l, except for TA which is expressed in meq/l and SO_4^{2-}/Cl^- expressed in mM/M. For a better visualization, the vertical scale of GP05PC was split 0–50/50–850 cm. Vertical green lines mark the level of methane saturation for seawater at 1 atm. For an improved visibility, methane concentration values of GP07BC were multiplied with a factor of 50. Horizontal blue and yellow bars show the SMTZ for cores GP07BC and GP05PC, respectively. At GP03PC sulfide values were below detection limit. Vertical arrows indicate seawater values. Deviating samples are denoted between brackets. ODP Leg 161 core-976D is used as reference core. (For interpretation of the references to colour in this figure legend, the reader is referred to the web version of this article.)
(Data from: Comas et al., 1999)

composition even though the sedimentary deposits consist of mud breccia. These observations are not only in contrast to the reference core ODP Leg 161 core-976D and core GP03PC containing hemipelagic sediments (Fig. 2b), but also to the mud-breccia interval immediately underlying these upper units (Figs. 7 and 8). All evidence points to rapid, recent, and non-steady state processes, including seawater infiltration into the mud breccia of the upper units. This will be discussed in detail in Sections 5.3 and 5.4.

5.2. Pore-water and gas sources for the lowermost mud-breccia intervals

The lowermost mud breccia from the summit cores GP07BC and GP05PC, show tendencies that are fully in line with the typical pore-water composition of anoxic MV sediments (Haese et al., 2006; Hensen

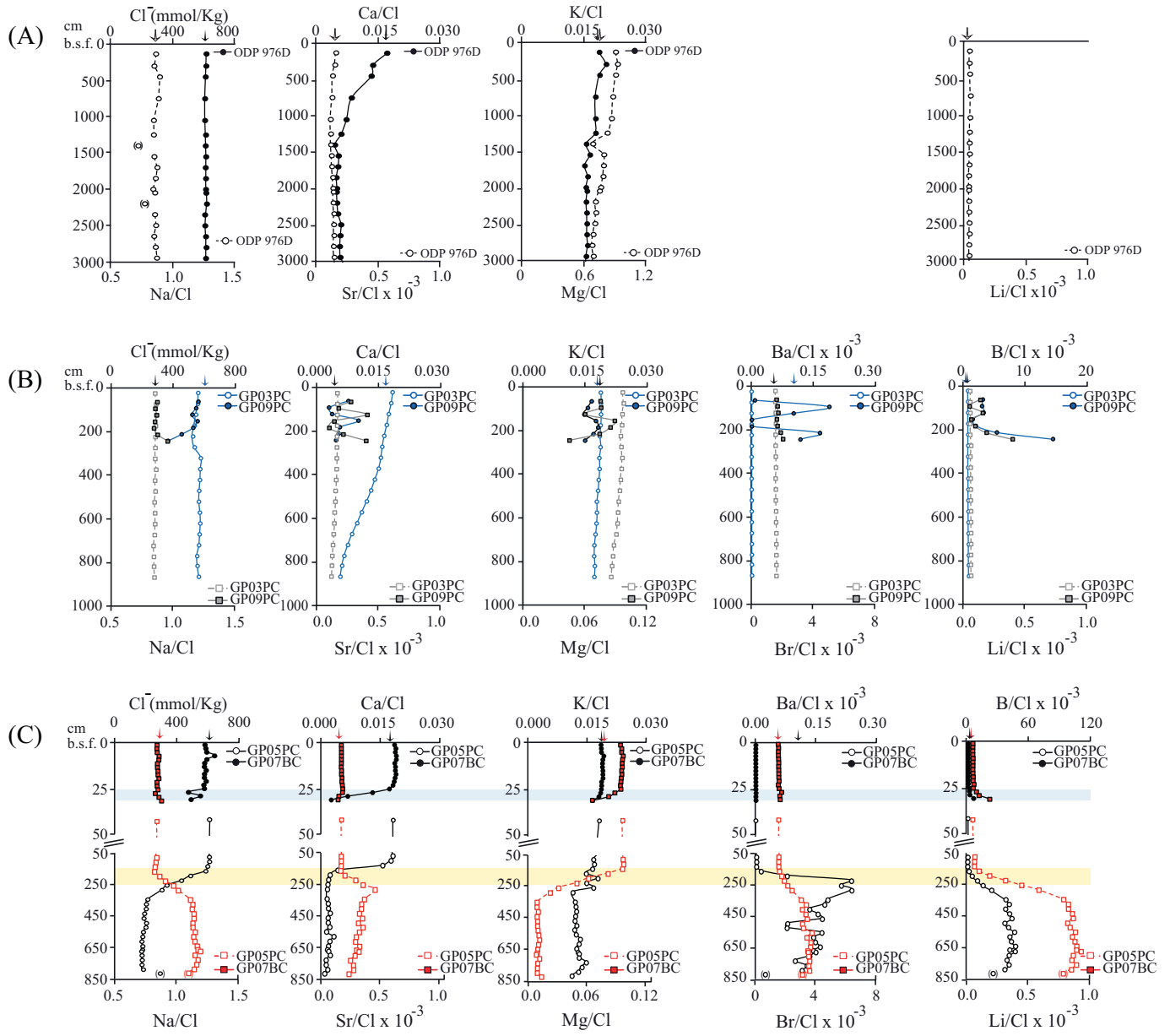

Fig. 8. Pore-water profiles for Cl^- (mM/kg), Ca/Cl, K/Cl (both M/M), Ba/Cl, B/Cl (both mM/M) for all investigated cores. Vertical arrows indicate seawater values. For a better visualization, the vertical scale of GP05PC was split 0–50/50–850 cm. Horizontal blue and yellow bars show the SMTZ for cores GP07BC and GP05PC, respectively. Deviating samples are denoted between brackets. ODP Leg 161 core-976D is used as reference core. (For interpretation of the references to colour in this figure legend, the reader is referred to the web version of this article.)
(Data from: Comas et al., 1999)

et al., 2007; Mazzini, 2009; Reitz et al., 2011).

The $\delta^{13}C_{methane}$ and $\delta D_{methane}$ observed in the lowermost breccia for the summit cores are consistent with biogenic gas possibly with admixture of gas of thermogenic origin; e.g., at GP05PC ($\delta^{13}C_{methane} \sim -58.5‰$ and $\delta D_{methane} \sim -179‰$), (Fig. 7; e.g., Schoell, 1980; Mastalerz et al., 2007, 2009; Etiope et al., 2011). In addition, the fairly constant methane isotopic values throughout the deep mud breccia interval reveal that this gas was not generated in situ, but rather derives from a deep source. This deduction fits well with $\delta^{13}C_{methane}$ data for core MS390G (Blinova et al., 2011) as well as with lipid biomarker data (López-Rodríguez et al., 2014). These indicate the presence of hydrocarbon gases (including methane) and hydrocarbon-derived compounds generated under favorable conditions for the formation of thermogenic gas during early stages of catagenesis.

For cores GP05PC and GP07BC, the lowermost pore-water profiles also reveal the presence of deep fluids, being strongly depleted in Cl^- and most other seawater components, but enriched in B, Li (Fig. 8). This low-salinity water may in general be related to: a. methane clathrate dissociation, b. meteoric water input, c. clay-membrane ion exchange, or d. clay-mineral dehydration processes (De Lange, 1983; Dählmann and De Lange, 2003; Hensen et al., 2004).

The stable oxygen ($\delta^{18}O_{pw}$) and hydrogen (δD_{pw}) isotopes of pore water are considered to be diagnostic for constraining the mechanisms affecting the freshening of pore fluids (Dählmann and De Lange, 2003). The deepest pore-fluid samples from our core GP05PC have a strong depletion in δD_{pw} and enrichment in $\delta^{18}O_{pw}$ (Fig. 9a and b), revealing a clearly negative correlation between them (Fig. 9a). This indicates that smectite to illite transformation takes place at greater depth, releasing fresh water (e.g. Dählmann and De Lange, 2003). Clay-mineral assemblages found at Carmen MV-cores (GP05PC, MS386G and MS390G)

Table 5
Element-based ratios calculated at the studied cores. TDS refers to total dissolved solids.

Depth (cm)	pH[a]	TDS (g/kg)	N/P
Hemipelagic GP03PC			
23	–	35.4	18
73	7.9	35.4	28
123	–	34.6	33
173	8.1	33.8	21
223	8.0	33.0	25
273	8.1	33.6	30
323	8.1	36.0	29
373	7.9	35.8	65
423	8.0	35.4	40
473	8.0	35.0	36
523	8.2	34.5	30
573	8.1	34.8	40
623	8.3	34.7	31
673	8.2	34.1	33
723	8.4	33.5	29
773	8.3	32.6	29
818	8.3	32.6	28
868	–	33.1	36
Carmen mud volcano GP05PC			
42	7.5	39.1	10
72	7.6	38.7	20
102	7.8	38.6	31
132	7.9	37.5	81
162	8.1	34.0	159
192	8.3	28.4	345
222	8.5	25.3	356
252	8.6	20.3	560
282	–	18.6	973
342	–	13.5	–
372	8.9	13.1	722
402	–	13.0	–
432	–	12.4	–
462	–	12.2	–
492	8.8	13.2	529
519	–	13.0	–
549	–	12.0	–
579	–	11.7	585
609	–	11.3	–
639	8.7	11.8	506
662	–	11.7	474
672	–	11.4	–
697	–	11.4	–
727	–	11.7	584
757	8.7	11.5	514
787	–	12.0	585
812	–	(18.9)	–
Carmen mud volcano GP07BC			
0	–		–
1	7.6	37.1	18
3	7.7	37.5	23
5	7.7	37.9	27
7	7.8	41.5	33
9	7.8	38.2	32
11	7.8	37.1	21
13	7.7	37.0	8
15	7.8	37.8	25
17	7.8	37.1	15
19	7.8	37.1	65
21	–	37.6	100
23	–	36.5	38
25	8.0	36.7	579
27	8.1	29.2	994
29	8.3	33.8	1013
31	–	29.6	644
Carmen mud volcano GP09PC			
63	7.9	33.6	381
93	7.9	31.5	343
123	7.9	30.1	11
153	7.9	33.5	37
183	7.9	31.4	41
213	7.9	26.6	93
243	8.0	21.8	294

[a] pH of porewater; measured pH may be enhanced for samples with enhanced dissolved inorganic carbon due to CO_2 degassing.

may support this interpretation, in particular the occurrence of randomly interstratified (R0) illite-smectite minerals (I/S) to more illitic ordered ones (R1–R3) (Fig. 4 and Table 4). However these also point to potential contributions from shallower sources.

5.2.1. Temperature and depth of fluid-formation processes

The smectite-to-illite transformation is thought to occur during burial diagenesis (e.g., Velde and Vasseur, 1992; Merriman and Peacor, 1999), taking place at greater depth and in a temperature range of 50 to 160 °C (e.g., Martin et al., 1996; Dählmann and De Lange, 2003; Hensen et al., 2004; Haese et al., 2006; Vazquez et al., 2016). Further indicators for temperatures of enhanced fluid-rock interactions can be derived from the bottom-most pore-water composition, which should have a near deep-fluid signature. Using equations based on empirical K-Na and K-Mg geo-thermometers (Haese et al., 2006 and references therein), we estimate an average temperature of formation of ~115 ± 15 °C for the deep fluids at Carmen MV (cf. Supplemental material).

In clay minerals, B and Li may act as exchangeable ions that can enter the interlayer and replace other cations (Bergaya et al., 2006). Such exchange may start in clay-rich sediments under relatively low temperatures (~50 °C; James et al., 2003; Aloisi et al., 2004) or burial diagenesis (Hensen et al., 2007; Scholz et al., 2010), and continue with increasing depth leading to significantly B- and Li-enriched fluids. Dissolved B and Li concentrations in pore water from the deeper portion of the sediment are highly enriched compared to seawater values (7.5 vs. 0.45 mmol/kg and 150 vs. 33 µmol/kg, respectively), further indicating a relatively high temperature for fluid/rock interaction (Martin et al., 1996; Kopf and Deyhle, 2002; Haese et al., 2003; Hensen et al., 2007; Scholz et al., 2009; Vanneste et al., 2011). A change in B- isotopes and concentration are thought to be associated with such smectite-illite transition (e.g. Mata et al., 2012).

The average clay-mineral dehydration temperature may also be derived using the pore-water $\delta^{18}O_{pw}$ and δD_{pw} composition and assuming equilibrium fractionation (after Hensen et al., 2004 and references therein). Accordingly, for a mud expulsion system near Costa Rica, a temperature of 85–135 °C was derived, and had a pore-water B-concentration of ~2 mM (Hensen et al., 2004). Using the same approach, and taking into account the enhanced B and Li content compared to that for Hensen et al. (2004) and for Scholz et al. (2010) in the Cadiz MV setting, we estimate a temperature of 100–150 °C for Carmen MV.

For the temperature of fluid formation, an alternative estimation can be made, based on the underlying smectite-to-illite transformation process. The occurrence of randomly interstratified (R0) illite-smectite (I/S) to more illitic (R1–R3) ordered minerals points to clay-mineral transformations taking place at a considerably wide range of depths from temperatures around 100 °C for the R0 I/S to 140–170 °C for the R1-R3 I/S (Vazquez et al., 2016). Such wide range of temperatures must be due to the entrainment of clay from different depths during the ascent of the deep material to the surface.

Thus, taking all evidence from elemental/isotope-geothermometer and clay-mineral derived temperatures together, this water-producing process is likely to take place predominantly at temperatures of 140 ± 20 °C. Using a regional geothermal gradient of 25–27 °C/km, and considering that geothermal gradients at active MVs may be larger, this temperature is reached at a maximum of ~5 km depth. This would correspond to the oldest and deepest over-pressurized units of the WAB (Unit VI–Unit Va - Early to Middle Miocene) at this site (Comas et al.,

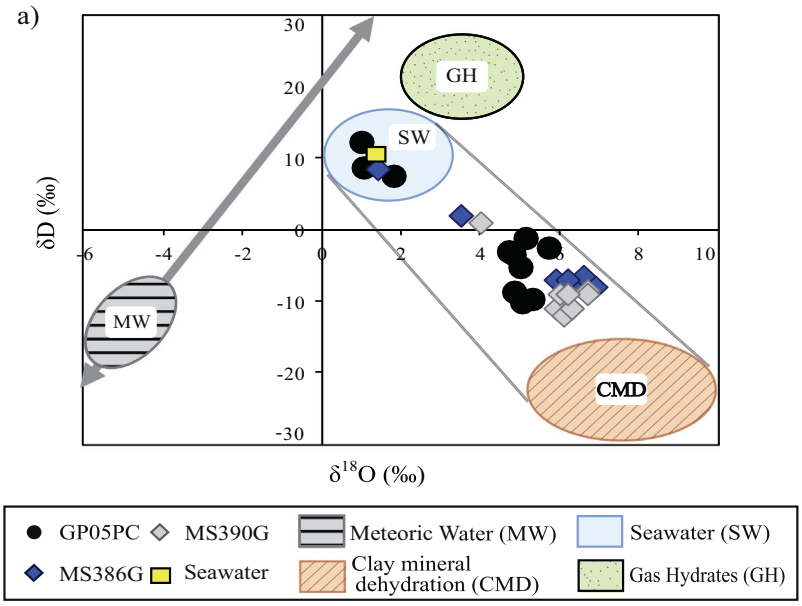

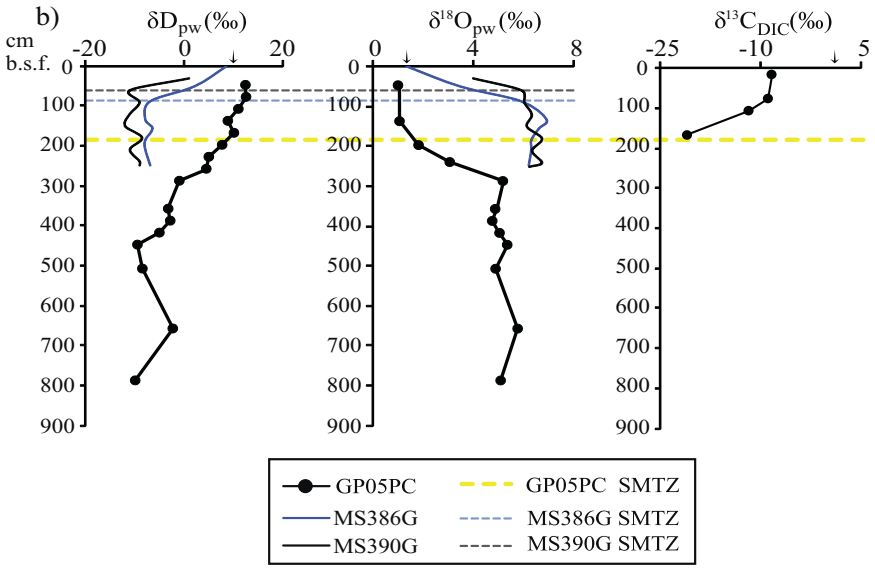

Fig. 9. a) Carmen MV δD_{pw} vs. $\delta^{18}O_{pw}$ values for core GP05PC (this study), for cores MS386G and MS390G (data from: Blinova et al., 2011), as well as for a Mediterranean deepwater from a CTD station taken above Carmen MV. Main fields affecting the δD_{pw} vs. $\delta^{18}O_{pw}$ composition of pore waters are presented as coloured circles (after Dählmann and De Lange, 2003). b) δD_{pw} and $\delta^{18}O_{pw}$ of pore water, and $\delta^{13}C$ of dissolved inorganic carbon (DIC) versus depth in core GP05PC from Carmen MV. Vertical arrows indicate seawater values. Yellow-, grey- and blue-dashed horizontal lines correspond to sulfate-methane transition zone (SMTZ) depths detected for cores GP05PC, MS390G, and MS386G, respectively. (For interpretation of the references to colour in this figure legend, the reader is referred to the web version of this article.)

1999; Talukder et al., 2003; Soto et al., 2010; Comas et al., 2012; López-Rodríguez et al., 2014). This conclusion is fully in line with previous, general geophysical observations, indicating that feeding channels of Alboran MVs connect with the oldest and deepest over-pressurized units overlying the metamorphic basement (Fig. 3b; i.e. Comas et al., 1999; Soto et al., 2010; Comas et al., 2012).

The strontium isotope ratio measured in the deep pore fluids from GP05PC is distinctly different from that in present-day Mediterranean seawater ($^{87}Sr/^{86}Sr$ 0.70901 ± 0.00002 for GP05PC vs. ~0.709165 ± 0.000010 for deep Mediterranean seawater; De Lange

Table 6
Summary of characteristic parameters for upper/lower units* porewater samples for core GP05PC.

	$^{87}Sr/^{86}Sr$	$\delta^{13}C_{DIC}$	$\delta^{18}O_{pw}$	δD_{pw}	TDS (mg/kg)[c]
Med-seawater	0.709165 ± 0.00001[a]	1.1 ± 0.0[b]	1.3 ± 0.1[b]	10 ± 1[b]	38.0 ± 0.3
Upper unit	–	−8.5 ± 0.0	1.0 ± 0.0	12 ± 1	38.5 ± 0.7
Lower unit	0.70901 ± 0.00002	nd	5.0 ± 0.0	−10 ± 7	12.0 ± 0.7

* Upper unit refers to the uppermost seawater-like interval; sample at 18 cm b.s.f. for $\delta^{13}C_{DIC}$ and 42 cm b.s.f. for δD and $\delta^{18}O$, whereas lower unit refers to the deep-fluid like lower interval; sample at 609 and 757 cm b.s.f. for $^{87}Sr/^{86}Sr$ average value, and 757 cm b.s.f. for δD and $\delta^{18}O$;. nd: not determined due to lack of sample.

[a] Average $^{87}Sr/^{86}Sr$ composition of Mediterranean seawater (from De Lange et al., 1990).

[b] Stable carbon, oxygen and hydrogen isotope correspond to averaged values of seawater samples recovered at GP08CT CTD Station taken above Carmen MV.

[c] Total dissolved solids (g/kg) calculated from total porewater composition; Mediterranean seawater of 37.976 salinity analyzed in the same series (n = 10), gave TDS of 38.0 ± 0.3; Upper unit (0–132 cm; n = 4); Lower unit (300–830 cm; n = 17).

et al., 1990) (Table 6). The observed value in GP05PC is similar to the value of seawater in the Late Miocene ($^{87}Sr/^{86}Sr$ ratio ~ 0.70899 ± 0.00002; Schildgen et al., 2014; De Lange et al., 1990). As Messinian evaporites have been reported to be absent in the WAB, and the pore-water salinity is very low but with relatively enhanced Sr (Sr/Cl) content (Fig. 8), recrystallization of Late Miocene carbonate is most likely producing this $^{87}Sr/^{86}Sr$. The high-pressure/temperature fluid-rock interaction consuming e.g. Ca (Sr) must then have masked the concomitant Ca (Sr) increase. However, we cannot fully exclude the possibility that the observed $^{87}Sr/^{86}Sr$ ratio in our pore water could be related to a contribution of 'crustal fluid´ as suggested for MVs in the Gulf of Cadiz (Hensen et al., 2015).

5.2.2. NH_4^+-generating processes

A major increase in the concentration of ammonium (NH_4^+) and phosphate (PO_4^{3-}) in core GP05PC is observed with depth. At this site, the downcore increase of these two species cannot be associated with in-situ organic matter (OM) degradation (Fig. 7). Within the cored interval, the OM content and degradation rates are too low to maintain this NH_4^+ profile, if a C:N:P Redfield-ratio of 106:16:1 is assumed. Furthermore the NH_4^+ and PO_4^{3-} distribution for cores GP05PC and GP07BC has an extremely high N/P ratio (N/P ~ 1000; Table 5). NH_4^+ build-up can also be related to mineral desorption processes (De Lange, 1992b). In addition, smectite-illite conversion and the associated rearrangement of interlayer cations, e.g. K^+ vs. NH_4^+, having a rather similar ionic radius (NH_4^+: 1.43 Å; K^+: 1.33 Å), could form an illite negative surface layer charge. Depending on the K^+/NH_4^+ content of the surrounding fluid phase, this may lead to fixing or releasing of K^+ or NH_4^+.

The above-derived temperature window for these processes (140 ± 20 °C) is also favorable for NH_4^+ release from decomposing OM at depth (*catagenesis*; e.g. Martin et al., 1996). This may be associated with methanogenesis, agreeing with data on gas composition and lipid biomarkers (Blinova et al., 2011; López-Rodríguez et al., 2014). However, this NH_4^+ release would be accompanied with PO_4^{3-} release. Catagenesis may thus only be the dominant process if a major sink for PO_4^{3-} occurs. The latter is not uncommon at a sulfate-methane transition zone (SMTZ) (e.g. März et al., 2008; Dijkstra et al., 2014; Liu et al., 2018). As a major NH_4^+ and a moderate PO_4^{3-} increase is observed, a predominant contribution from a combination of these processes is likely.

In any case, all evidence points to a deep source for the expelled fluids from Carmen MV.

5.3. Transition between upper, seawater-intruded and lower, deep-fluid-related interval

Below the interval with seawater-like pore-water composition, there is a rapid change to deep-source composition in the summit cores GP05PC and GP07BC (Figs. 7 and 8). The lower boundary for this transition is located at 200 cm depth for core GP05PC and is extrapolated/estimated to occur at ~35 cm for core GP07BC (Figs. 8 and 9b). The rapid depletion of sulfate indicates that sulfate-reduction driven by anaerobic oxidation of methane (AOM) takes place at these levels (Fig. 7). This interpretation is supported by the enhanced concentration of HS^- between ~50 and 200 cm depth in core GP05PC and at 25 cm in core GP07BC (Fig. 7), i.e. the depth interval where the SMTZ occurs. In both cores a sharp increase in methane concentrations takes place below the SMTZ to values above its sea-level saturation value (~900 μM; Fig. 7). In addition, the gradient toward isotopically light $\delta^{13}C_{DIC}$ observed in GP05PC is consistent with methane oxidation occurring at this transition.

The large amount of DIC produced during AOM processes may also induce authigenic carbonate formation. This leads to the associated consumption of calcium and bicarbonate in a ratio of 1:2, reducing the pore-water Ca^{2+} and DIC contents in a 1:2 ratio (i.e. Hensen et al., 2007; Reitz et al., 2011). The deepest pore fluids from core GP05PC are strongly depleted in dissolved Ca^{2+} and Mg^{2+}, as indicated by Ca/Cl and Mg/Cl ratios below the SMTZ (Fig. 8). This fact may point to authigenic carbonate precipitation. The DIC isotopic composition (~ −21‰; Fig. 9b) indicates anaerobic oxidation of OM/CH_4 as a source for DIC. The DIC excess production then outpaces $CaCO_3$ precipitation. Modeling results agree with this interpretation, with depth-integrated rates of $CaCO_3$ precipitation ($2.32 \cdot 10^{-5}$ mol/cm^2 yr) being lower than DIC production ($3.34 \cdot 10^{-5}$ mol/cm^2 yr). Thus excess DIC-production and $CaCO_3$-precipitation predominantly takes place at the SMTZ depth (Fig. 5). However, the low Ca^{2+}, Mg^{2+} and high DIC in the lower-most unit are predominantly related to a deep source provenance.

5.4. Origin and timing for the seawater-like signature in the upper mud-breccia interval

The clear seawater-like composition including the absence of biogeochemical reaction products (e.g., PO_4^{3-}, NH_4^+, DIC) in the uppermost mud-breccia sediments (see Section 5.1) all point to a relatively recent process for the summit cores from Carmen MV. This is most prominently evident for core GP05PC, where consistent seawater-like pore-water concentrations and elemental/isotopic ratios occur above the sulfate-reduction zone (Figs. 7–9). This tendency strongly suggests a very recent downward intrusion of bottom seawater. A similar but shallower downward entrainment of bottom water is evident for core GP07BC.

Comparable geochemical patterns have been described for MVs from the Eastern Mediterranean (Mastalerz et al., 2007; Feseker et al., 2010) and the Black Sea (Reitz et al., 2011), where hydrocarbon gas ebullition or bioirrigation by tube-dwelling organisms were evoked as potential factors. Hypothetically, there are a few processes that could in general lead to such seawater-like composition in uppermost sediments. These are I) mass movement of sediments, such as sliding and/or slumps; II) release of gas due to depressurization upon core recovery; III) bioirrigation by tube-dwelling organisms; IV) hydrocarbon gas ebullition from deeper units or V) mud-flow deposition and degassing.

I. The recent deposition of sediments promoted by mass movements through slope features such as slumps or sliding may lead to a seawater-like composition of the pore water in the uppermost interval (Zabel and Schulz, 2001; Hensen et al., 2003; Hong et al., 2014). For Carmen MV such slumping can be excluded not only because of its bathymetric position but also as its uppermost sediments have the same deep MV-related origin, i.e. mud breccia, as the lowermost sediments.
II. As major degassing occurs due to depressurization upon core recovery, this might be a scenario resulting in changes in the pore-water signature within the uppermost interval. However, the observed pore-water profiles and species concentrations, e.g. the absence of methane in the uppermost interval, are inconsistent with a recovery-related release. In addition, the amount of gas and bottom water that may be exchanged for such limited sediment column is insufficient to create the major and distinct offset observed.
III. Bio-irrigation of uppermost sediments can contribute to the exchange between deep pore fluids and overlying bottom water and may extend for several meters into the sediments (e.g., Weaver and Schultheiss, 1983; Fossing et al., 2000; Haese et al., 2003, 2006). In Carmen MV this process might exclusively affect the uppermost breccia intervals (from 0 to 10 cm depth), since specific chemosynthetic epifauna were found only above ~10 cm depth. In addition, to replace > 95% of pore fluid and dissolved constituents, would require very intense or long-lasting irrigation.
IV. The occurrence of continuous or pulsed hydrocarbon gas ebullition, i.e. without mud expulsion, at faults or gas hydrate formation/destabilization sites may lead to concomitant downward entrainment

of seawater and thus to sea-water-like composition of pore waters within the uppermost interval (Tryon et al., 1999, 2002; Haeckel et al., 2007; Mastalerz et al., 2007; Chuang et al., 2013; Hong et al., 2016).

The absence of any substantial hemipelagic draping for all studied Carmen MV summit cores as well as the deep-sourced, entirely mud breccia composition, excludes this option.

For some MVs active methane fluxes for central areas have been observed and entrainment of bottom water into the immediately surrounding sediment has been postulated (Mastalerz et al., 2007; Feseker et al., 2010; Reitz et al., 2011). Under this scenario of continuous hydrocarbon release we would expect to find at least somewhat enhanced methane and ammonia concentrations in the uppermost sediments, which is not the case. In addition, this would require a vigorous methane flux as driving force for such entrainment. In contrast to Isis MV (Mastalerz et al., 2007), such major methane flux into the water column was not observed for Carmen MV. Therefore, such scenario is not likely in this case.

V. A mud breccia expulsion event of overpressurized deep sedimentary units must be accompanied by rigorous degassing. Hence, this can be considered as an extreme gas-ebullition event compared to scenarios III and IV above.

For immobile sediment/fluid structures and upward advecting/bubbling gas alone, elegant modeling has been done to demonstrate steady-state required methane fluxes, associated sulfate reduction rates and depths of downward advecting bottom water (e.g. scenarios III, IV; Fossing et al., 2000; Haeckel et al., 2007). In the present case, there is clear evidence for mud breccia expulsion at the summit of Carmen MV. This involves the upward advection of overpressurized deep sediment, fluid and gas onto the seafloor and its subsequent rapid degassing of massive amounts of methane. Haeckel et al. (2007) used hypothetical methane bubble-train cylinders/tubes with diameter of 1 cm and reached bottom water concentrations within a few years for a tube spacing of 18 cm between these. Within the tubes instantaneous replacement with bottom water was anticipated. A more dense spacing will lead to a more rapid replacement by bottom water for the upper sediment unit. Consequently, the rapid degassing of outflowing overpressurized mud at Carmen MV must have resulted in a rapid, 'instantaneous' replacement of pore fluid by bottom water in the upper sediments. Oxygen associated with this bottom water is rapidly consumed together with methane, and any remaining methane is oxidized using sulfate, resulting in a $\delta^{13}C_{DIC}$ that is substantially lower than in seawater for this upper unit (Figs. 7 and 9b).

Possibly the penetration depth of bottom water into the mud breccia may be dictated by the duration of gas release which itself may relate to the thickness of the deposited mudflow and its actual gas content.

This scenario would adequately explain the deep-fluid mudflow-related pore-water composition in the lower part, and the bottom-water-like composition in the upper part of the recovered sediments. The lack of hemipelagic draping, the constant bottom water-level concentrations nearly without biochemical reaction products, and the sharp transition to the underlying unit, all point to a very recent event. In view of the side-scan-sonar observations-derived recent mudflow outline (Fig. 3a), this could well be related to the same mudflow extrusion event. Subsequent to its deposition, at the interface between sulfate-rich upper and methane-rich lower sediments an AOM front develops, and diffusion of dissolved species along the concentration gradient starts. The excess upward methane-flux results in the rapidly upward-retreating sulfate boundary, whereas the slower molecular diffusion-controlled inert- ion concentrations more slowly adapt (e.g. Cl^-, Fig. 6; see also difference in depth of gradient for Mg/Cl and SO_4^{2-}/Cl; Figs. 7 and 8). This difference is reproduced in the modeling study from core GP05PC, whereby a sharp model front develops during the ebullition (with methane having a smoother front due to gas dissolution during the ebullition (Fig. 5, blue lines). The development of the model from this sharp transition toward its current state is not the same for all species, as reactive species retain a steeper transition due to reaction processes as compared to conservative species such as Cl^-.

A rapid and very recent mudflow/hydrocarbon expulsion event is not only evident in cores GP05PC and GP07BC, but also for GP09PC. In the latter core, the enhanced SO_4^{2-}/Cl^- in the hemipelagic unit at 120–131 cm, indicates that the overlying mud breccia must also have been very recently deposited. These observations and the sonograph image showing a recent mudflow (low backscatter signature), all suggest that this refers to the same recent mudflow, most of which was deposited from the very summit into an eastward direction.

Transport pathways and mechanisms can best be evaluated while using conservative (non-reactive) elements such as Cl^-. The Cl^- vs. depth profile has a dramatic shift at ~195 cm in core GP05PC (Figs. 5 and 6). Assuming an abrupt mud-expulsion event and an initial, idealized block-shaped profile (t = 0; Fig. 6), the subsequent development of the Cl^- profile vs. time can be evaluated. For core GP05PC, the development of the simulated conservative Cl^- concentration versus depth profile clearly points to a very recent timing of the eruptive event.

The current situation is reached surprisingly quickly, in a period of only 12 years (± 5 years) (Fig. 6). This indicates that this eruptive event took place very recently, i.e. in the year 2000 CE ± 5 yr. This could partly explain the somewhat larger activity observed during the June-2008 TTR-17 Logachev-cruise compared to our November-2011 GASALB-Pelagia cruise.

This mud-eruption event nearly coincides with a major earthquake in this region (i.e., Al Hoceima earthquake in 2004). Onset of methane gas ebullition due to earthquakes has been previously reported (e.g. Tsunogai et al., 2012; Fischer et al., 2013). However, we do not want to speculate that all MV eruptions may be related to earthquakes. Further studies correlating detailed geochemical and geophysical regional data are necessary to fully corroborate this interesting hypothesis for this seismically active region.

6. Conclusions

A recent mudflow expulsion followed by gas ebullition and associated bottom water infiltration into mud breccia sediment at Carmen MV has resulted in a pore-water composition that is distinctly characterized by a seawater-like uppermost and a deep-fluid-like lowermost interval.

The origin for the reduced salinity in the lowermost pore waters in cores GP05PC and GP07BC is related to clay-mineral dehydration, i.e. smectite-illite conversion, taking place at greater depth. Adequate paleo-thermometers applied to the elemental and isotope ratios of this deep water, result in a rather well-defined formation temperature of ~140 ± 20 °C. Taking a regional geothermal gradient of 25–27 °C/km, this suggests a fluid source from ~5 ± 1 km depth. This corresponds to the depth interval of overpressured shales and megabreccias from the West-Alboran basin (Units VI–Va, - Early to Middle Miocene) from which feeding channels appear to emanate upward. The Late-Miocene $^{87}Sr/^{86}Sr$-derived age for the Sr dissolved in the lowermost pore waters is consistent with these sedimentary mud-source units.

The distinct pore-water profiles and the quantitative transport and reaction model, have permitted to accurately determine the timing of the mud breccia expulsion event to have taken place very recently, in the year 2000 CE ± 5 yrs.

Acknowledgments

The authors gratefully acknowledge the GASALB-Pelagia Shipboard Party, technicians as well as Captain and crew of *R/V* Pelagia for support and collaboration during the cruise as well as TTR-17 Leg 1 Shipboard Party and *R/V* Professor Logachev Captain and crew. We thank H. De Haas for providing cruise technical details and J.M.R

Alpiste for multibeam data processing. In addition, we thank the Pelagia shipboard scientific party and in particular K. Bakker and S. Ossebaar for on-board nutrient analyses, D. Gallego-Torres, D. Apostolova, and L. López-Alcaide for on-board methane and alkalinity analyses. A. van Dijk is thanked for his helpful assistance during stable isotopes analyses, C. van der Veen and T. Röckmann at IMAU - laboratory for methane isotope analyses, and P. Böning and K. Pahnke at ICBM, University of Oldenburg, for Sr isotope determination. Special thanks go to R. Hennekam, M.L. Goudeau and E. Grimoldi for their work and nice cooperation in pore-water extractions and sub-sampling. This work was supported by MINECO Spanish Projects [CTM2009-07715, CGL2011-1441, CGL2012-32659 and CGL2015-66830-R]; and the Andalusian Government Research Group [RNM-179 and RNM-215]. C. F. López-Rodríguez was funded by a JAE-PhD fellowship from the CSIC (Spain); she acknowledges subsequent funding from the STSM in the framework of COST action ES1301.

Appendix A. Supplementary data

Supplementary data to this article can be found online at https://doi.org/10.1016/j.margeo.2018.11.013.

References

Aloisi, G., Wallmann, K., Bollwerk, S.M., Derkachev, A., Bohrmann, G., Suess, E., 2004. The effect of dissolved barium on biogeochemical processes at cold seeps. Geochim. Cosmochim. Acta 68, 1735–1748. https://doi.org/10.1016/j.gca.2003.10.010.

Bergaya, F., Theng, B.K.G., Lagaly, G., 2006. Handbook of Clay Science, 1st edition. Elsevier Publication, Amsterdam.

Blinova, V.N., Comas, M.C., Ivanov, M.K., Poludetkina, E.N., Matveeva, T.V., 2011. Active mud volcanism in the West Alboran Basin: geochemical evidence of hydrocarbon seepage. Mar. Pet. Geol. 28, 1483–1504. https://doi.org/10.1016/j.marpetgeo.2011.06.001.

Boudreau, B.P., 1997. Diagenetic models and their implementation. Mar. Pet. Geol. 15, 279. https://doi.org/10.1016/S0264-8172(98)80005-6.

Boudreau, B.P., Ruddick, B.R., 1991. On a reactive continuum representation of organic matter diagenesis. Am. J. Sci. 291. https://doi.org/10.2475/ajs.291.5.507.

Brass, M., Röckmann, T., 2010. Continuous-flow isotope ratio mass spectrometry method for carbon and hydrogen isotope measurements on atmospheric methane. Atmos. Meas. Tech. 3, 1707–1721. https://doi.org/10.5194/amt-3-1707-2010.

Chuang, P.-C., Dale, A.W., Wallmann, K., Haeckel, M., Yang, T.F., Chen, N.-C., Chen, H.-C., Chen, H.-W., Lin, S., Sun, C.-H., You, C.-F., Horng, C.-S., Wang, Y., Chung, S.-H., 2013. Relating sulfate and methane dynamics to geology: accretionary prism offshore SW Taiwan. Geochem. Geophys. Geosyst. 14 (7), 2523–2545. https://doi.org/10.1002/ggge.20168.

Comas, M.C., Zahn, R., Klaus, A., 1996. Proceedings of the Ocean Drilling Program, Initial Reports, 161. Mediterranean Sea II, the Western Mediterranean, Leg 161. Ocean Drilling Program, College Station, TX.

Comas, M.C., Platt, J.P., Soto, J.I., Watts, A.B., 1999. The origin and tectonic history of the Alboran Basin: insights from Leg 161 results. In: Zahn, R., Comas, M.C., Klaus, A. (Eds.), Proceedings of the Ocean Drilling Program, Scientific Results. vol. 161. Ocean Drilling Program, College Station, TX, pp. 555–580.

Comas, M., Pinheiro, L.M., Ivanov, M., 2010. The Alboran Sea (Leg 1): look into mud volcanoes, carbonate mounds and climate changes. In: IOC Tech. Ser., vol. 94. UNESCO, pp. 8–63.

Comas, M.C., Suades, E., Crespo-Blanc, A., 2012. From mud diapirs to mud volcanoes: shale tectonics within the structural evolution of the Alboran Sea basin. Geotemas 13, 138–141.

Dählmann, A., De Lange, G.J., 2003. Fluid-sediment interactions at Eastern Mediterranean mud volcanoes: a stable isotope study from ODP Leg 160. Earth Planet. Sci. Lett. 212, 377–391. https://doi.org/10.1016/S0012-821X(03)00227-9.

De Lange, G.J., 1983. Geochemical evidence of a massive slide in the southern Norwegian Sea. Nature 305, 420–422.

De Lange, G.J., 1992a. Shipboard routine and pressure-filtration system for pore-water extraction from suboxic sediments. Mar. Geol. 109, 77–81. https://doi.org/10.1016/0025-3227(92)90221-3.

De Lange, G.J., 1992b. Distribution of exchangeable, fixed, organic and total nitrogen in interbedded turbiditic/pelagic sediments of the Madeira Abyssal Plain, eastern North Atlantic. Mar. Geol. 109, 95–114. https://doi.org/10.1016/0025-3227(92)90223-5.

De Lange, G.J., Boelrijk, N.A.I., Catalano, G., Corselli, C., Klinkhammer, G., Middelburg, J., Müller, D., Ullman, W., Van Gaans, P., Woittiez, J.R., 1990. Sulphate related equilibria in the hypersaline brines of the Tyro and Bannock Basins, eastern Mediterranean. Mar. Chem. 31, 89–112. https://doi.org/10.1016/0304-203(90)90032-8.

Dijkstra, N., Kraal, P., Kuypers, M.M.M., Schnetger, B., Slomp, C.P., 2014. Are iron-phosphate minerals a sink for phosphorus in anoxic Black Sea sediments? PLoS One 9 (7), e101139. https://doi.org/10.1371/journal.pone.0101139.

Etiope, G., Schoell, M., Hosgormez, H., 2011. Abiotic methane flux from the Chimaera seep and Tekirova ophiolites (Turkey): understanding gas exhalation from low temperature serpentinization and implications for Mars. Earth Planet. Sci. Lett. 30, 96–104. https://doi.org/10.1016/j.epsl.2011.08.001.

Feseker, T., Brown, K.R., Blanchet, C., Scholz, F., Nuzzo, M., Reitz, A., Schmidt, M., Hensen, C., 2010. Active mud volcanoes on the upper slope of the western Nile deep-sea fan—first results from the P362/2 cruise of R/V Poseidon. Geo-Mar. Lett. 30, 169–186. https://doi.org/10.1007/s00367-010-0192-0.

Fischer, D., Mogollón, J.M., Strasser, M., Bohrmann, G., Fekete, N., Spiess, V., Kasten, S., 2013. Subduction zone earthquake as potential trigger of hydrocarbon seepage. Nat. Geosci. 6, 647–651. https://doi.org/10.1038/NGEO1886.

Fisher, R., Lowry, D., Wilkin, O., Sriskantharajah, S., Nisbet, E.G., 2006. High-precision, automated stable isotope analysis of atmospheric methane and carbon dioxide using continuous-flow isotope-ratio mass spectrometry. Rapid Commun. Mass Spectrom. 20, 200–208. https://doi.org/10.1002/rcm.2300.

Fossing, H., Ferdelman, T.G., Berg, P., 2000. Sulfate reduction and methane oxidation in continental margin sediments influenced by irrigation (South-East Atlantic off Namibia). Geochim. Cosmochim. Acta 64, 897–910. https://doi.org/10.1016/S0016-7037(99)00349-X.

Grasshoff, K., Ehrhardt, K., Kremling, K., 1983. Methods of seawater analysis. Verlag Chemie, Weinheim, New York.

Haeckel, M., Boudreau, B.P., Wallmann, K., 2007. Bubble-indiced por water mixing: a 3-D model for deep porewater irrigation. Geochim. Cosmochim. Acta 71, 5134–5154. https://doi.org/10.1016/j. gca.2007.08.011.

Haese, R.R., Meile, C., Van Cappellen, P., De Lange, G.J., 2003. Carbon geochemistry of cold seeps: methane fluxes and transformation in sediments from Kazan mud volcano, eastern Mediterranean Sea. Earth Planet. Sci. Lett. 212, 361–375. https://doi.org/10.1016/S0012-821X(03)00226-7.

Haese, R.R., Hensen, C., De Lange, G.J., 2006. Pore water geochemistry of eastern Mediterranean mud volcanoes: implications for fluid transport and fluid origin. Mar. Geol. 225, 191–208. https://doi.org/10.1016/j.margeo.2005.09.001.

Hensen, C., Zabel, M., Pfeifer, K., Schwenk, T., Kasten, S., Riedinger, N., Schulz, H.D., Boetius, A., 2003. Control of sulfate pore-water profiles by sedimentary events and the significance of anaerobic oxidation of methane for the burial of sulfur in marine sediments. Geochim. Cosmochim. Acta 67, 2631–2647. https://doi.org/10.1016/S0016-7037(03)00199-6.

Hensen, C., Wallmann, K., Schmidt, M., Ranero, C.R., Suess, E., 2004. Fluid expulsion related to mud extrusion off Costa Rica - a window to the subducting slab. Geology 32, 201–204. https://doi.org/10.1130/G20119.1; 5.

Hensen, C., Nuzzo, M., Hornibrook, E., Pinheiro, L.M., Bock, B., Magalhães, V.H., Brückmann, W., 2007. Sources of mud volcano fluids in the Gulf of Cadiz—indications for hydrothermal imprint. Geochim. Cosmochim. Acta 71, 1232–1248. https://doi.org/10.1016/j.gca.2006.11.022.

Hensen, C., Scholz, F., Nuzzo, M., Valadares, V., Gracia, E., Terrinha, P., Liebetrau, V., Kaul, N., Silva, S., Martinez-Loriente, S., Bartolome, R., Pinero, E., Magalhaes, V.H., Schmidt, M., Weise, S.M., Cunha, M., Hilario, A., Perea, H., Rovelli, L., Lackschewitz, K., 2015. Strike-slip faults mediate the rise of crustal-derived fluids and mud volcanism in the deep sea. Geology 43, 339–342. https://doi.org/10.1130/G36359.1.

Hong, W.-L., Solomon, E.A., Torres, M.E.A., 2014. Kinetic-model approach to quantify the effect of mass transport deposits on pore water profiles in the Krishna–Godavari basin, Bay of Bengal. Mar. Pet. Geol. 58, 223–232.

Hong, W.-L., Torres, M.T., Carroll, J., Cremiere, A., Panieri, G., Yao, H., Serov, P., 2016. Seepage from an arctic shallow marine gas hydrate reservoir is insensitive to momentary ocean warming. Nat. Commun. 8, 15745. https://doi.org/10.1038/ncomms15745.

Howarth, R.J., McArthur, J.M., 1997. Statistics for strontium isotope stratigraphy: a robust LOWESS fit to marine Sr-isotope curve for 0 to 206 Ma, with look-up table for derivation of numeric age. J. Geol. 105, 441–456. https://doi.org/10.1086/515938.

Ivanov, M.K., Kenyon, N.H., Laberg, J.S., Blinova, V.N., 2010. Cold seeps, coral mounds and deep-water depositional systems of the Alboran Sea, Gulf of Cadiz and Norwegian continental margin. In: IOC Tech. Ser., vol. 94 UNESCO.

James, R.H., Allen, D.E., Seyfried, W.E., 2003. An experimental study of alteration of oceanic crust and terrigenous sediments at moderate temperatures (51 to 350 °C): insights as to chemical processes in near-shore ridge-flank hydrothermal systems. Geochim. Cosmochim. Acta 67 (4), 681–691. https://doi.org/10.1016/S0016-7037(02)01113-4.

Jurado, M.J., Comas, M.C., 1992. Well log interpretation and seismic character of the Cenozoic sequence in the Northern Alboran Sea. Geo-Mar. Lett. 12, 129–136. https://doi.org/10.1007/BF02084923.

Kopf, A.J., Deyhle, A., 2002. Back to the roots: boron geochemistry of mud volcanoes and its implications for mobilization depth and global B cycling. Chem. Geol. 192, 195–210. https://doi.org/10.1016/S0009-2541(02)00221-8.

Liu, J., Wang, J., Izon, G., Antler, G., Wang, Z., Zhao, J., Egger, M., 2018. Vivianite formation in methane-rich deep-sea sediments from the South China Sea. Biogeosci. Discuss. https://doi.org/10.5194/bg-2018-340. (in review).

López-Rodríguez, C., Stadnitskaia, A., De Lange, G.J., Martínez-Ruíz, F., Comas, M., 2014. Origin of lipid biomarkers in mud volcanoes from the Alboran Sea, western Mediterranean. Biogeosciences 11, 3187–3204. https://doi.org/10.5194/bg-11-3187-2014.

Lueker, T.J., Dickson, A.G., Keeling, C.D., 2000. Ocean pCO2 calculated from dissolved inorganic carbon, alkalinity, and equations for K1 and K2: validation based on laboratory measurements of CO2 in gas and seawater at equilibrium. Mar. Chem. 70, 105–119. https://doi.org/10.1016/S0304-4203(00)00022-0.

Martin, B., Kastner, M., Henry, P., Le Pichon, X., Lallement, S., 1996. Chemical and isotopic evidence for sources of fluids in a mud volcano field seaward of the Barbados accretionary wedge. J. Geophys. Res. 101, 20.325–20.345.

Martin-Ramos, 2006. XPowder. Programa para análisis cualitativo y cuantitativo por

difracción de rayos X. Macla 4–5, 35–44.
März, C., Hoffmann, J., Bleil, U., De Lange, G.J., Kasten, S., 2008. Diagenetic changes of magnetic and geochemical signals by anaerobic methane oxidation in sediments of the Zambezi deep-sea fan (SW Indian Ocean). Mar. Geol. 255, 118–130. https://doi.org/10.1016/j.margeo.2008.05.013.
Mastalerz, V., De Lange, G.J., Dählmann, A., Feseker, T., 2007. Active venting at the Isis mud volcano, offshore Egypt: origin and migration of hydrocarbons. Chem. Geol. 246, 87–106. https://doi.org/10.1016/j.chemgeo.2007.09.005.
Mastalerz, V., De Lange, G.J., Dählmann, A., 2009. Differential aerobic and anaerobic oxidation of hydrocarbon gases discharged at mud volcanoes in the Nile deep-seafan. Geochim. Cosmochim. Acta 73, 3849–3863. https://doi.org/10.1016/j.gca.2008.12.030.
Mata, P., Williams, L.B., Nieto, F., Martos, R., Sáinz-Díaz, C.I., 2012. Preliminary B and Li isotope data of illite/smectite from mud volcano sediments from the Gulf of Cádiz. Macla 16, 100–101.
Mazzini, A., 2009. Mud volcanism: processes and implications. Mar. Pet. Geol. 26, 1677–1680. https://doi.org/10.1016/j.marpetgeo.2009.05.003.
Merriman, R.J., Peacor, D.R., 1999. Very low-grade metapelites: mineralogy, microfabrics and measuring reaction progress. In: Frey, M., Robinson, D. (Eds.), Low-Grade Metamorphism. Blackwell Science, pp. 19–60. https://doi.org/10.1002/9781444313345.ch2.
Milkov, A., 2000. Worldwide distribution of submarine mud volcanoes and associated gas hydrates. Mar. Geol. 167 (1–2), 29–42. https://doi.org/10.1016/S0025-3227(00)00022-0.
Mogollón, J.M., Dale, A.W., Fossing, H., Regnier, P., 2012. Timescales for the development of methanogenesis and free gas layers in recently-deposited sediments of Arkona Basin (Baltic Sea). Biogeosciences 9, 1915–1933. https://doi.org/10.5194/bg-9-1915-2012.
Moore, D.M., Reynolds Jr., R.C., 1997. X-ray Diffraction and the Identification and Analysis of Clay Minerals. Oxford Uni. Press, United Kingdom (378 pp.).
Nelson, S., 2000. Sample vial influences on the accuracy and precision of carbon and oxygen isotope ratio analysis in continuous flow mass spectrometric applications. Rapid Commun. Mass Spectrom. 14, 293–297. https://doi.org/10.1002/(SICI)1097-0231(20000229)14:4<293::AID-RCM869>3.0.CO;2-L.
Nieto, F., Arroyo, X., Arostegui, J., 2016. XRD-TEM-AEM comparative study of n-alkylammonium smectites and interstratified minerals in shallow-diagenetic carbonate sediments of the Basque-Cantabrian Basin. Am. Mineral. 101 (1–2), 385–398. https://doi.org/10.2138/am-2016-5301.
Petschick, R., 2004. http://www.geol-pal.uni-frankfurt.de/Staff/Homepages/Petschick/classicsoftware.html#MacDiff.
Reitz, A., Pape, T., Haeckel, M., Schmidt, M., Berner, U., Scholz, F., Liebetrau, V., Aloisi, G., Weise, S.M., Wallmann, K., 2011. Sources of fluids and gases expelled at cold seeps offshore Georgia, eastern Black Sea. Geochim. Cosmochim. Acta 75, 3250–3268. https://doi.org/10.1016/j.gca.2011.03.018.
Sapart, C.J., van der Veen, C., Vigano, I., Brass, M., van de Wal, R.S.W., Bock, M., Fischer, H., Sowers, T., Buizert, C., Sperlich, P., Blunier, T., Behrens, M., Schmitt, J., Seth, B., Röckmann, T., 2011. Simultaneous stable isotope analysis of methane and nitrous oxide on ice core samples. Atmos. Meas. Tech. 4, 2607–2618. https://doi.org/10.5194/amt-4-2607-2011.
Schildgen, T.F., Cosentino, D., Frijia, G., Castorina, F., Dudas, F.O., Iadanza, A., Sampalmieri, G., Cipollari, P., Caruso, A., Bowring, S.A., Strecker, M.R., 2014. Sea level and climate forcing of the Sr isotope composition of late Miocene Mediterranean marine basins. Geochem. Geophys. Geosyst. 2964–2983. https://doi.org/10.1002/2014GC005332.
Schoell, M., 1980. The hydrogen and carbon isotopic composition of methane from natural gases of various origins. Geochim. Cosmochim. Acta 44, 649–661. https://doi.org/10.1016/0016-7037(80)90155-6.
Scholz, F., Hensen, C., Reitz, A., Romer, R.L., Liebetrau, V., Meixner, A., Weise, S.M., Haeckel, M., 2009. Isotopic evidence (87Sr/86Sr, δ7Li) for alteration of the oceanic crust at deep-rooted mud volcanoes in the Gulf of Cadiz, NE Atlantic Ocean. Geochim. Cosmochim. Acta 73, 5444–5459. https://doi.org/10.1016/j.gca.2009.06.004.
Scholz, F., Hensen, C., De Lange, G.J., Haeckel, M., Liebetrau, V., Meixner, A., Reitz, A., Romer, R.L., 2010. Lithium isotope geochemistry of marine pore waters – insights from cold seep fluids. Geochim. Cosmochim. Acta 74, 3459–3475. https://doi.org/10.1016/j.gca.2010.03.026.
Seeberg-Elverfeldt, J., Schlüter, M., Feseker, T., Martin, K., 2005. Rhizon sampling of porewaters near the sediment-water interface of aquatic systems. Limnol. Oceanogr. 3, 361–371. https://doi.org/10.4319/lom.2005.3.361.
Soetaert, K., Meysman, F., 2012. Reactive transport in aquatic ecosystems: rapid model prototyping in the open source software R. Environ. Model. Softw. 32, 49–60. https://doi.org/10.1016/j.envsoft.2011.08.011.
Soetaert, K., Meysman, F., Petzoldt, T., 2010. Solving differential equations in R. AIP Conf. Proc. 1281, 31–34. https://doi.org/10.1063/1.3498463.
Somoza, L., Medialdea, T., León, R., Ercilla, G., Vázquez, J.T., Farran, M., Hernández-Molina, J., González, J., Juan, C., Fernández-Puga, M.C., 2012. Structure of mud volcano systems and pockmarks in the region of the Ceuta Contourite Depositional System (Western Alboran Sea). Mar. Geol. 332–334, 4–26. https://doi.org/10.1016/j.margeo.2012.06.002.
Soto, J.I., Fernández-Ibáñez, F., Talukder, A.R., Martínez-García, P., 2010. Miocene shale tectonics in the northern Alboran Sea (Western Mediterranean). AAPG Mem. 119–144. https://doi.org/10.1306/13231312M933422.
Stoll, M.H.C., Bakker, K., Nobbe, G.H., Haese, H.H., 2001. Continuous-flow analysis of dissolved inorganic carbon content in seawater. Anal. Chem. 73 (17), 4111. https://doi.org/10.1021/ac010303r.
Talukder, A.R., Comas, M.C., Soto, J.I., 2003. Pliocene to Recent mud diapirism and related mud volcanoes in the Alboran Sea (Western Mediterranean). Geol. Soc. Lond. Spec. Publ. 216, 443–459. https://doi.org/10.1144/GSL.SP.2003.216.01.29.
Tryon, M.D., Brown, K.M., Torres, M.E., Trehu, A.M., McManus, J., Collier, R.W., 1999. Measurements of transience and downward fluid flow near episodic methane gas vents, Hydrate Ridge, Cascadia. Geology 27, 1075–1078. https://doi.org/10.1130/0091-7613(1999)027<1075:MOTADF>2.3.CO;2.
Tryon, M.D., Brown, K.M., Torres, M.E., 2002. Fluid and chemical flux in and out of sediments hosting methane hydrate deposits on Hydrate Ridge, OR, II: hydrological processes. Earth Planet. Sci. Lett. 201, 541–557. https://doi.org/10.1016/S0012-821X(02)00732-X.
Tsunogai, U., Maegawa, K., Sato, S., Komatsu, D.D., Nakagawa, F., Toki, T., Ashi, J., 2012. Coseimic massive methane release from a submarine mud volcano. Earth Planet. Sci. Lett. 341–344, 79–85. https://doi.org/10.1016/j.epsl.2012.06.004.
Vanneste, H., Kelly-Gerreyn, B.A., Connelly, D.P., James, R.H., Haeckel, M., Fisher, R.E., Heeschen, K., Mills, R.A., 2011. Spatial variation in fluid flow and geochemical fluxes across the sediment–seawater interface at the Carlos Ribeiro mud volcano (Gulf of Cadiz). Geochim. Cosmochim. Acta 75, 1124–1144. https://doi.org/10.1016/j.gca.2010.11.017.
Vazquez, M., Bauluz, B., Nieto, F., Morata, D., 2016. Illitization sequence controlled by temperature in volcanic geothermal systems: the Tinguiririca geothermal field, Andean Cordillera, central Chile. Appl. Clay Sci. 134, 221–234. https://doi.org/10.1016/j.clay.2016.04.011.
Velde, B., Vasseur, G., 1992. Estimation of the diagenetic smectite-to-illite transformation in time-temperature space. Am. Mineral. 77, 967–976.
Weaver, P.P.E., Schultheiss, P.J., 1983. Vertical open burrows in deep-sea sediments, 2 m in length. Nature 310, 329–331. https://doi.org/10.1038/301329a0.
Zabel, M., Schulz, H.D., 2001. Importance of submarine landslides for non-steady state conditions in pore water systems - lower Zaire (Congo) deep-sea fan. Mar. Geol. 176, 87–99. https://doi.org/10.1016/S0025-3227(01)00164-5.